universität wien

MASTERARBEIT / MASTER'S THESIS

Titel der Masterarbeit / Title of the Master's Thesis

„Simulations and design of a quadrupole bender for annihilation studies with slow extracted antiprotons“

verfasst von / submitted by

Marcus Bumbar, BSc

angestrebter akademischer Grad / in partial fulfilment of the requirements for the degree of

Master of Science (MSc)

Wien, 2023 / Vienna, 2023

Studienkennzahl lt. Studienblatt / degree programme code as it appears on the student record sheet:	UA 066 876
Studienrichtung lt. Studienblatt / degree programme as it appears on the student record sheet:	Masterstudium Physics / Master's degree program Physics
Betreut von / Supervisor:	Hon.-Prof. Dipl.-Phys. Dr. Eberhard Widmann

Kurzfassung

Gegenwärtig ist die Antiprotonen-Nukleus Annihilation bei niedrigen kinetischen Energien ein Prozess, der noch nicht vollkommen verstanden wird. Des Weiteren wurden die am häufigsten verwendeten Simulationsprogramme Geant4 und FLUKA für Hochenergiephysik-Anwendungen entwickelt und deren Ergebnisse stimmen nicht mit den gemessenenen Daten für niedrige Energien überein. Aus diesem Grund wird ein neues Projekt am ASACUSA-CUSP experiment am CERN durchgeführt, welches darauf abzielt, die Annihilationsprozesse von Antiprotonen mit einem Set von repräsentativen Atomkernen zu messen und die existierenden Modelle dadurch zu validieren, aber auch bisher unbekannte Eigenschaften wie die Multiplizität von bei der Antiprotonenannihilation entstehenden Pionen zu ermitteln. Um dies zu bewerkstelligen wird eine Strahlführung für kontinuierlich extrahierte Antiprotonen entwickelt, deren Design auf die Verwendung von elektrostatischen Quadrupol Deflektoren und Einzel-Linsen basiert. Diese Arbeit präsentiert die Ergebnisse der Simulationen für den gesamten zurückgelegten Weg der Teilchen von der Falle bis zur Annihilation am Target, welche mit der SIMION Software durchgeführt wurden. Das Ziel jener Simulationen ist es eine 90° Richtungsänderung des Strahles zu ermöglichen und gleichzeitig Teilchen- oder Qualitätsverluste am Strahl auf ein Minimum zu begrenzen. Die Optimierung des Aufbaus wurde unter der Verwendung diverser Techniken, wie Simplex Optimierung für Potentiale und Sweeps für die Verbesserung der Geometrie, durchgeführt.

Abstract

At present antiproton-nucleus annihilation at rest is a process that is not well understood. Furthermore, the most commonly used simulation models such as Chiral Invariant Phase Space model (CHIPS) and Fritiof precompound model (FTFP) in GEANT4 and the peanut model in FLUKA were developed for high energy physics application and disagree with the scarce data. Therefore, a new project is being conducted at the ASACUSA-Cusp experiment at CERN to measure antiproton-nucleus annihilation for a representative set of nuclei, aiming to validate the existing nuclear models but to also reveal hitherto unknown features for most nuclei such as the total multiplicity of emitted pions. For this reason, a beam line for the transport of slow extracted antiprotons is being constructed. The design relies on bending and focusing elements, including an electrostatic quadrupole deflector and steering Einzel lenses. This thesis will present simulations of the full antiproton beam path, starting from the particle trap all the way to the annihilation target, which were carried out using SIMION simulation software. The aim of these simulations is to achieve a design capable of a 90° bend, creating a beam with a diameter smaller than the target foil, and with minimal transmission losses. The optimization of the geometry and the applied voltages was achieved using a combination of several methods, such as geometry sweeps and the the Nelder-Mead method.

Acknowledgements

I would like to extend my gratitude to Eberhard for his supervision and for providing me with the invaluable opportunity to work at the SMI and in ASACUSA.

For Angela's unwavering motivation, continuous support, and guidance throughout this project I am tremendously grateful. Her dedication, particularly in proofreading, was critical for the completion of this thesis. With her meticulous attention to detail she elevated the quality of this work.

For further feedback and corrections on my thesis I would also like to thank Dan. The impact he, Eric and Andreas had on me by introducing me to working in a lab and welcoming me at CERN is something profound thanks have to be offered for. My time working with them has been an incredibly enriching experience, and I am sincerely thankful for their guidance and support throughout my journey.

I would also like to express my heartfelt appreciation to Hannes, Martin, and Doris for their willingness to generously provide explanations whenever I encountered challenges. Their expertise and insights have been immensely valuable in expanding my knowledge and understanding.

To Alina, Amit, Carina, Kaku, Lilian, Marlene, Simon and Viktoria I want to express my sincere thanks for not only being my colleagues but also for becoming my friends. The time spent as team gold will never be forgotten. A special thanks again to Viktoria, for helping me with LaTeX since 2016.

Lastly, I wish to express my heartfelt gratitude to Zuzanna for the time she sacrificed, her encouragement and humor. You always found the right words to motivate me.

Contents

1. Introduction

1.1. Motivation

CPT symmetry refers to charge conjugation, parity transformation and time reversal, the only combination of discrete symmetries that is still exact within experimental limits in modern particle physics. Its invariance implies that particles and antiparticles have the same or sign-opposite intrinsic properties. This leads to the assumption, that the amount of matter and antimatter created in the Big Bang must be the same. However, the observation that there is an asymmetry in the absolute quantities of matter and antimatter is one of the biggest unsolved mysteries of modern physics. The so called Baryon asymmetry lacks a quantitative explanation in the standard model of particle physics (SM) [1]. For this reason the study of antimatter and its possible deviations from the theoretical predictions are of great interest.

At the Antimatter Factory at the European Organization for Nuclear Research (CERN) multiple experiments are being conducted with the purpose of testing CPT predictions either by looking for differences in the structure of antimatter and matter by laser or microwave spetroscopy [2, 3, 4] or the gravitational acceleration [5, 6]. The majority of these experiments detect antihydrogen or antiprotons by measuring the annihilation products. For efficient detection and correct tagging of events, the antiproton-nucleus ($\overline{\mathrm{p}}$A) annihilation is the most important process to design the experiments' detectors. Simulations are needed to discriminate detected events from the background, for which the most frequently used models are the Chiral Invariant Phase Space model (CHIPS) and Fritiof precompound model (FTFP) included in Geometry and Tracking (GEANT4) [7, 8, 9, 10, 11], and the PEANUT model [12] used in Fluktuierende Kaskade model (FLUKA) [13]. One downside of these models is that they all have been developed for high energy physics applications and were only extrapolated to low energies, which are relevant for the AD experiments, using theoretical models. Additionally, none of the models were developed using annihilation data on nuclei, but rather on single nucleons. As shown in fig. 1.1 the models created this way do not describe the existing data for $\overline{\mathrm{p}}$A correctly. The multiplicities of minimum ionizing particles (MIP), mostly pions, and heavily ionizing particles (HIP), particles with masses equal to or higher than the proton mass, differ from the numbers predicted by the current models for annihilation at rest. Further measurements at lower energies are necessary to improve the understanding of $\overline{\mathrm{p}}$A annihilations and to improve the models within the Monte Carlo simulations.

For this reason a dedicated set-up for annihilation studies is being constructed at the

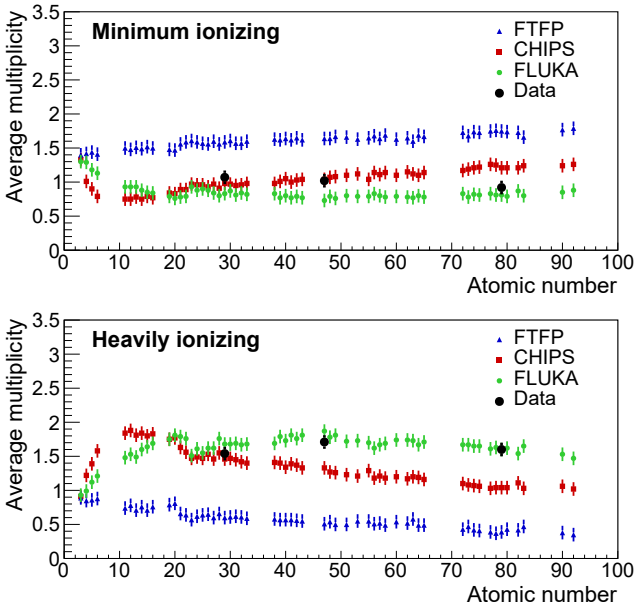

Figure 1.1.: Measured particle multiplicity from antiproton annihilations as a function of atomic number for MIPs (top) and HIPs (bottom) by the Antihydrogen Experiment: Gravity, Interferometry, Spectroscopy (AEGIS) experiment at CERN [14]. In black the three results for copper silver and gold are visible with the statistical error marked. Based on the $\mathrm{d}E/\mathrm{d}x$ classifications the error bars for the simulations are drawn.

Atomic Spectroscopy And Collisions Using Slow Antiprotons (ASACUSA) experiment by modifying an existing beam-line to transport slow, i.e. continuously extracted antiprotons to various targets. Ultimately the $\overline{\mathrm{p}}\mathrm{A}$ annihilation process will be investigated by measuring the energies of the annihilation products and the multiplicities using Timepix4 detectors [15]. To make these measurements possible, the work of this thesis consists of designing and simulating a number of ion optics, which enabled the construction of the necessary beam optics elements.

1.2. Antimatter Annihilation

Annihilation is a process that occurs when antimatter and matter come into contact with each other. The initial particles are transformed and no longer exist in their original form. A variety of possible outcomes of the annihilation processes can occur depending on the particles and energies involved. Products of a particular annihilation are restricted by the conservation of charge, linear and angular momentum, and total energy. When, for instance, an electron (e^-) and a positron (e^+), two elementary particles, interact at low energies, they produce two gamma-ray photons. For this example to not contradict

the conservation of linear momentum and total energy, it requires the production of at least two photons that are emitted back to back. With composite particles consisting of multiple quarks, such as nucleons and anti-nucleons, the annihilation process gains in complexity.

The antiproton-nucleon annihilation ($\overline{\mathrm{p}}$N) at low energies can produce different numbers of pions at rest. The measured pion multiplicities of the proton-antiproton annihilation ($\mathrm{p}\overline{\mathrm{p}}$) can be seen in table 1.1 and fig. 1.2.

Table 1.1.: Measured pion multiplicity for proton-antiproton annihilations, data from [16].

resulting number of pions	[%]
2	0.38 ± 0.03
3	7.4 ± 0.3
4	18.1 1.8
5	35.2 ± 3.7
6	23.3 ± 2.8
7	3.3 ± 0.3

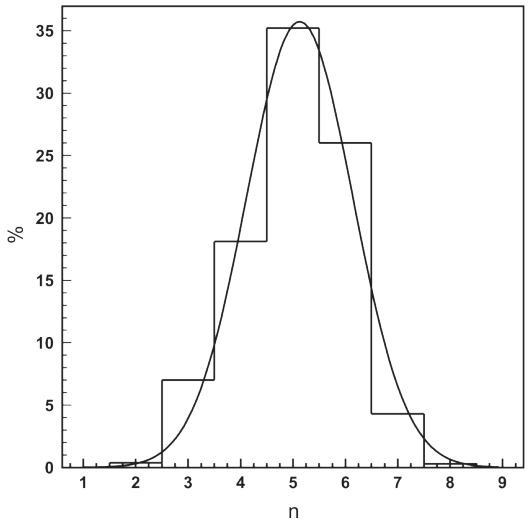

Figure 1.2.: Plot of the pion multiplicity distribution with measured values and a Gaussian fit applied to the data set. Plot taken from [16].

The annihilation of an antiproton with a neutron happens in a similar way, the results differ however because of the different quark compositions and the total charge.

The antiproton-nucleus annihilation takes place after an $\overline{\mathrm{p}}$ is captured in a bound atomic orbit and cascades downwards. While doing so, X-rays and Auger electrons are emitted

[17]. This process continues until the $\overline{\mathrm{p}}$ arrives at the surface of the nucleus. Here in most cases antiproton annihilation on one nucleon takes place and depending on their energy the products of this annihilation can further penetrate the nucleus [18]. This process is not well understood yet and requires further investigation as the data from measurements and the results from simulations exhibit a non-negligible discrepancy [14].

This thesis is organized as follows: in the following chapter an overview of the ASACUSA experiment is presented. This is done by first explaining the process of producing and decelerating antiprotons in the AD, followed by a short description of the main experiment and then further explaining the trapping and the slow extraction of the antiprotons. Chapter three recaps the physics background necessary for trajectory calculation and the design process of the ion optics. In Chapter five a few of the configurations based on the work in chapter four are compared, while also providing insights into the production process of the corresponding parts. In the last chapter a short summary followed by an outlook for the annihilation experiment is given.

2. The ASACUSA experiment

2.1. The Antiproton Decelerator

The Antiproton Decelerator (AD) is a 180 m circumference ring at CERN, used for the deceleration of the antiprotons produced by collisions of high energy protons with a target. This production method leads to antiprotons exhibiting a high kinetic energy (E_{kin}). A multi-step deceleration of the particles is necessary to minimize beam emittance and to make the particles usable for several experiments that study antiprotons or antihydrogen in the AD-hall [19].

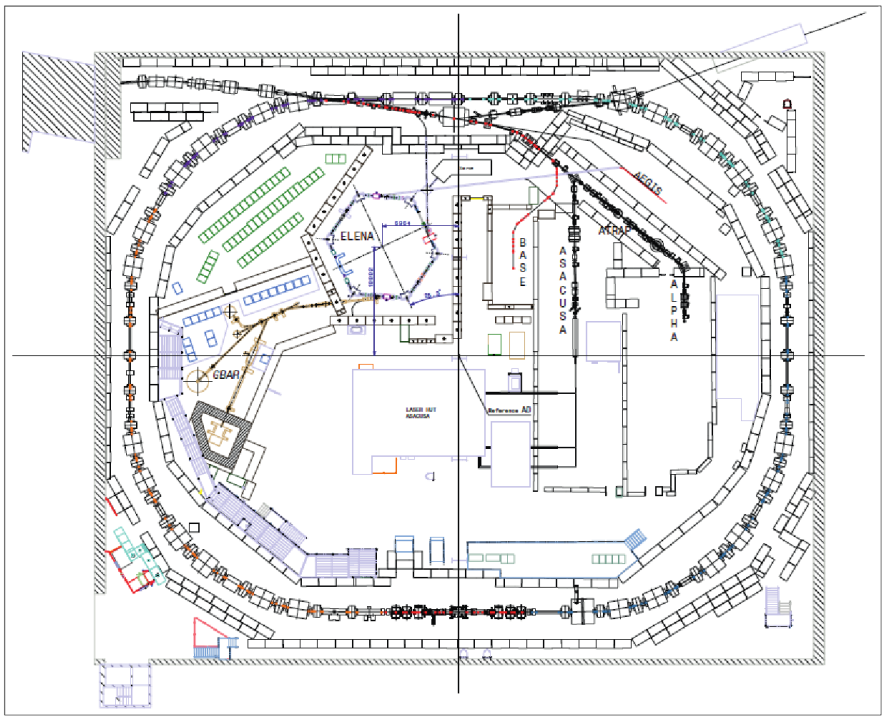

Figure 2.1.: Schematic view of the AD-Hall with the position of ELENA and the experiments marked. Figure from [20].

The deceleration process for each shot injected into the AD consists of four main steps shown in fig. 2.2:

1. **Production and Injection**
   A 50 mm-long Ir target is struck by a pulsed beam of protons at 36 GeV from the

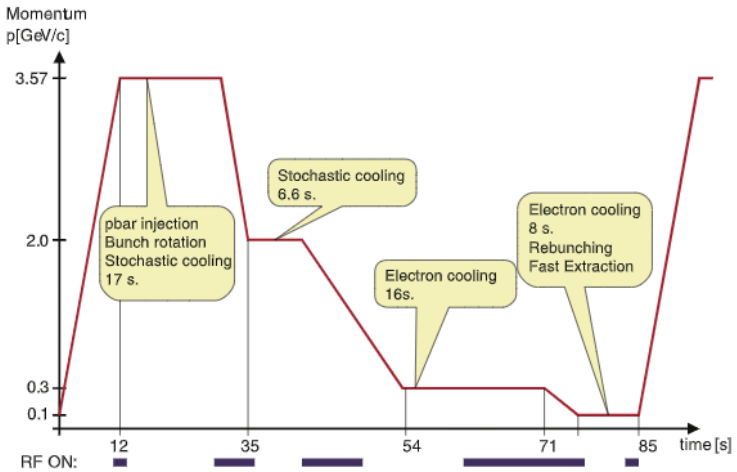

Figure 2.2.: A schematic view of the AD antiproton deceleration cycle (red). Figure from [19].

Proton Synchrotron (PS). Each shot produces 5×10^7 $\overline{\text{p}}$ at 3.57 GeV/c. Thereafter these particles are focused by a magnetic horn-type lens into a parallel beam and injected into the AD.

2. **RF bunch rotation**
   The bunches are then stretched in length by a RF field. The relative momentum $\Delta p/p$ of the antiprotons is reduced to about 1.5%.

3. **Stochastic cooling and deceleration**
   "Pickup" electrodes detect deviations in the momentum Δp_i and the position Δx_i of subgroups of $\overline{\text{p}}$ relative to all orbiting $\overline{\text{p}}$. By applying electric pulses with steering electrodes, the subgroups are corrected, focused and afterwards further decelerated with the use of RF-cavities. This reduces $\Delta p/p$ to 0.07% and p to 2 GeV/c.

4. **Electron cooling**
   The antiprotons are decelerated to $p = 300$ MeV/c and then merged with an e^- beam in a 2 m-long section. Their velocities are matched, so that the $\overline{\text{p}}$ can transfer their kinetic energy via Coulomb collisions to the e^-. After another deceleration step to $p = 100$ MeV/c, electron cooling is applied for a second time before extraction.

Approximately 3×10^7 $\overline{\text{p}}$ with an energy of 5.3 MeV are ejected from the AD after each cycle.

2.2. Extra Low Energy Antiproton ring (ELENA)

Trapping particles requires the electrodes of the traps to be set to potentials proportional to the particles' kinetic energy. Therefore, limiting the antiprotons' E_{kin} to a few keV is

necessary. Before ELENA, this part of the deceleration was carried out using a series of degrading foils, and in the case of ASACUSA a radio frequency quadrupole decelarator (RFQD) was additionally employed [21]. By first decelerating particles that were fulfilling the phase condition in its cavity, the RFQD reduced the energy of the particles, allowing about 30% of each AD-pulse to reach the foils with energies of 120 keV. Annihilations with said foils were responsible for a loss of around 99% of the pulse ejected from the AD, while still permitting the transmission of some particles with energies too high for trapping. Furthermore, deceleration with foils is a statistical process depending on a particles path through the medium. This effect introduces an energy dispersion proportional to the thickness of the traversed medium and is referred to as straggling. It can negatively impact the quality of the beam and has to be accounted for in the experiments.

By the introduction of the additional smaller ring ELENA, which operates in a similar albeit shorter cycle than the AD, the antiprotons are decelerated from the AD's 5.3 MeV down to 100 keV. The advantages of ELENA are on one hand a higher deceleration efficiency, and on the other hand its capability to provide pulses of $\overline{\mathrm{p}}$ on a cycle to cycle basis [22]. Before, the beam was shared among the experiments in 8-hour shifts, leading to frequent interruptions of the measurements performed by each experiment.

2.3. Experimental setup

Atomic Spectroscopy And Collisions Using Slow Antiprotons (ASACUSA) is one of the experiments situated at the AD. The main purpose of the experiment is to test the CPT theorem by measuring the hyperfine-splitting in antihydrogen. The schematic diagram from fig. 2.3 shows the paths the particles travel in the experiment and the dots show where each of the respective particles are trapped. The part with reduced opacity on the right side depicts the antihydrogen ($\overline{\mathrm{H}}$) production and spectroscopy region of the experiment. The production of the $\overline{\mathrm{H}}$ for the main experiment takes place in the Cusp-trap, named after the shape of the magnetic field lines. By using two sets of anti Helmholtz configuration coils and a multi ring electrode trap (MRE), antiprotons and positrons are confined in the same nested potential well and are combined into $\overline{\mathrm{H}}$. At the top of the picture the location of the foil and detector for the annihilation experiment is shown. The antiprotons travel from ELENA and enter MUSASHI, where they are trapped. After slow extraction from MUSASHI the antiprotons are deflected and transported through the positron beam-line towards the target.

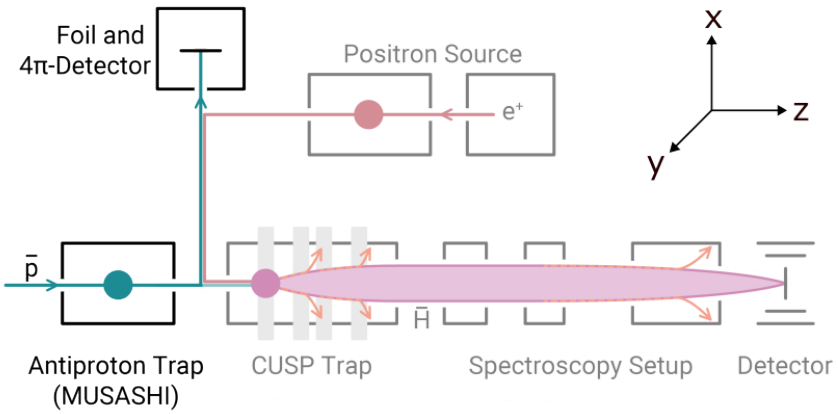

Figure 2.3.: Schematic diagram of the ASACUSA experiment. The paths traversed by $\overline{\mathrm{p}}$ are depicted in teal, e^+ in red, antihydrogen in magenta.

For the purpose of this thesis, the coordinate system defined in fig. 2.3 will be utilized.

2.4. Monoenergetic Ultra Slow Antiproton Source for High-precision Investigations (MUSASHI)

As the 100 keV beam provided by ELENA still exhibits E_{kin} too high for experiments relying on low energy $\overline{\mathrm{p}}$, its pulses have to be further adjusted for the ASACUSA experiment. As the experiment's trapping procedure was optimized for 120 keV during the RFQD-era, the particles from ELENA have to be accelerated for it to be compatible with the biaxially oriented polyethylene terephtalate (BO-PET) foils, that function as beam profile monitors and degraders [23]. This acceleration from 100 keV to 120 keV is achieved with a drift tube located between ELENA and MUSASHI.

After passing the foils antiprotons are trapped within MUSASHI. A combination of electrostatic and magnetic fields is used in this kind of traps for the confinement of particles. The electrostatic field is generated by a set of cylindrical electrodes that are arranged co-axially around the trap's central axis. These electrodes are held at different voltages, which creates an electric field that is parallel to the axis of the trap.

The electric field provides the force for the longitudinal confinement, while the magnetic field, generated by solenoid magnets that are arranged in a cylindrical configuration around the trap, are required for the confining force that prevents the charged particles

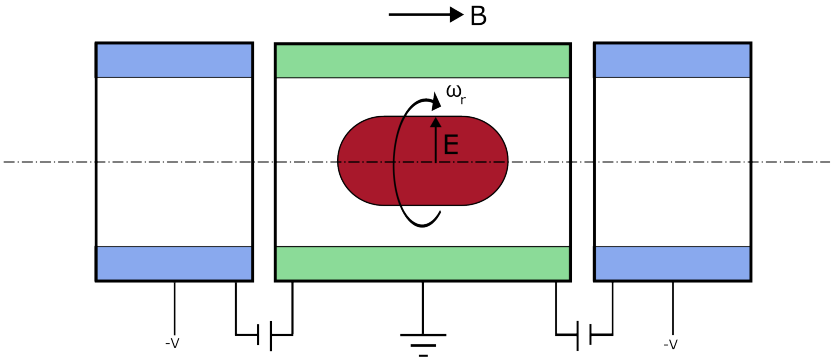

Figure 2.4.: Schematic drawing of a Penning-Malmberg trap for antiprotons. The particles are confined in the area marked in red in the center of the trap.

from escaping radially [24]. The magnetic field in the trap is homogeneous and runs parallel to its axis. A simplified schematic diagram of a Penning-Malmberg trap is depicted in fig. 2.4. The motion of a charged particle in such a combination of fields consists of different components. On the one hand, it is reflected between the potentials of the trapping well, while the magnetic field induces a rotational motion based on the Lorentz force acting on the particle. The components of this motion as well as the combination of these can be seen in fig. 2.5.

MUSASHI uses an additional rotating wall technique which involves rapidly changing the applied voltages on a split cylindrical electrode. This rotation creates a time-varying electric field that causes the charged particles to move in a circular orbit around the axis of the trap. This circular motion in turn can help to improve the confinement of the particles by reducing the plasma's radial expansion, which results in fewer collisions with the walls of the trap [25].

MUSASHI's solenoid produces a 2.5 T strong field in its trapping region. Its MRE, depicted in fig. 2.6, is located in the homogeneous part of its magnetic field. It is capable of both extracting pulses of antiprotons for the $\overline{\mathrm{H}}$ experiment, as well as providing a slow extraction mode, necessary for annihilation experiments.

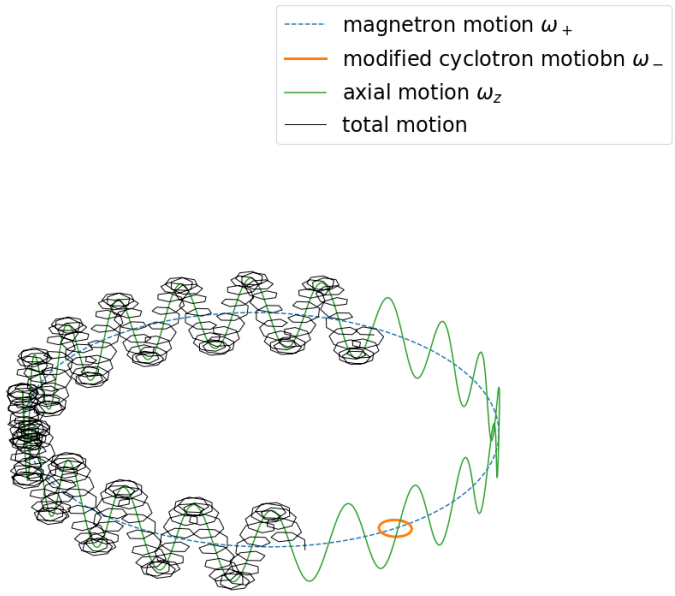

Figure 2.5.: Schematic representation of the different motions performed and overlayed in black on part of the diagram the resulting total motion of a charged particle in a Penning-Malmberg trap. By carefully tuning the parameters, particles can be kept in Penning-Malmberg traps for extended periods of time.

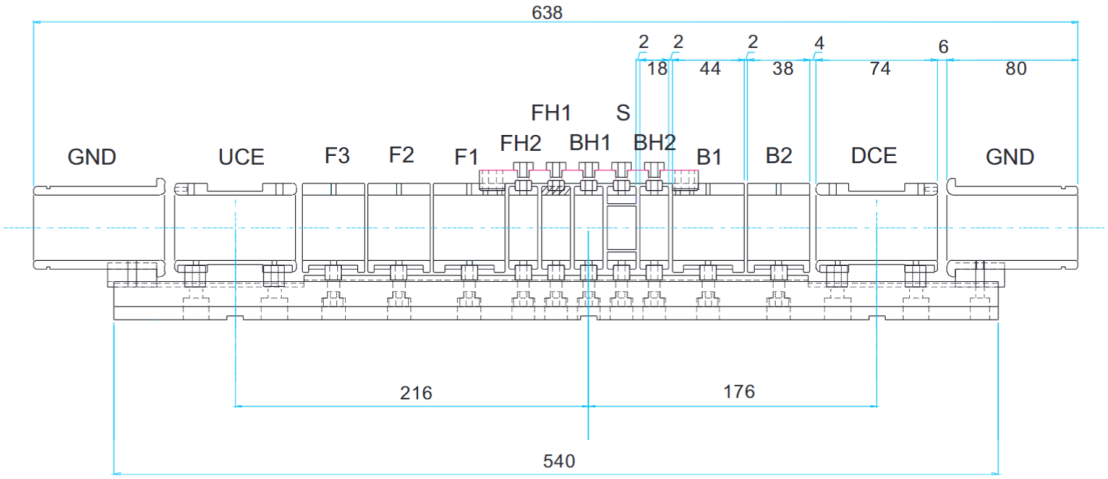

Figure 2.6.: Schematics of MUSASHI's MRE-trap composed of cylindrical electrodes [26].

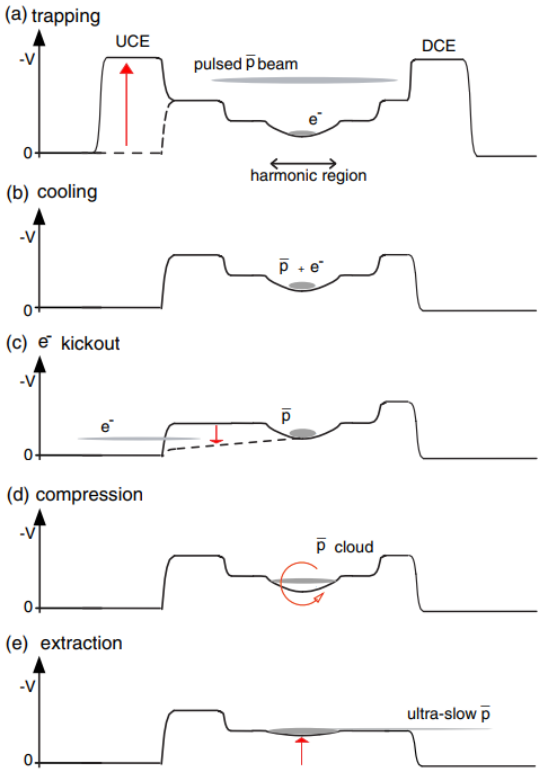

Figure 2.7.: Antiproton trapping, cooling, electron kick-out, compression, and extraction procedures performed in MUSASHI. Figure taken from [24].

The procedures applied to each shot that is trapped by MUSASHI and the subsequent steps for the slow extraction are depicted in fig. 2.7. To trap a shot, a potential of 13 kV is applied to the downstream catching electrode (DCE) as seen in fig. 2.7(a). This reflects the pulsed antiprotons back upstream, towards the upstream catching electrode (UCE). After the antiproton pulse enters MUSASHI and passes the MRE, the UCE is also ramped up to the same potential as the DCE, thereby reflecting the particles back and forth between these outermost electrodes. This process sets the outermost limits of the trapping field and has to be switchable in a few µs.

In fig. 2.7(b) the process of colliding the $\overline{\mathrm{p}}$ with a e^- plasma is shown. Here, similar to the process described in section 2.1, the antiprotons lose energy to the electrons. The e^- then in turn lose their energy by emitting cyclotron radiation.

Removing the e^-s from the plasma (as seen fig. 2.7(c)) is done by switching the trapping potential off long enough as to kick-out the electrons but for a short enough time as to not lose the $\overline{\mathrm{p}}$, because of their higher mass and therefore higher inertia.

In fig. 2.7(d) the split electrodes are then used to further compress the antiprotons by

using a rotating wall technique. By varying the potentials applied to the electrodes of the split electrode in the kHz range, the plasma can be set into motion and forced to turn around the z-axis of the trap. This greatly increases not only the time the particles can be stored in the trap, but also the number of antiprotons that can be extracted from the trap [24].

Fig. 2.7(e) shows how the $\overline{\mathrm{p}}$ are slowly extracted from the center of the MRE. By setting the ring electrodes neighboring the well potential, called the barrier potential, to a constant value during the extraction process, the desired E_{kin} can be achieved. The well potential of the MRE in the middle of MUSASHI is slowly raised, thereby raising the E_{pot} of the $\overline{\mathrm{p}}$, until they match the potential of the constant barrier potential. Because the particles exhibit an energy spread in transverse direction, they are then released in a direct current (DC) like manner, depending on their energy. The flux of particles can be controlled by how fast the well potential is ramped up to match the barrier potential. This beam of particles is then transported by a set of extraction electrodes (EE) and magnetic coils.

2.5. Transport coils and the positron beam-line and

The transport of the particles is aided by the use of magnetic field coils. The specifications and positions of the three coils between MUSASHI and the Cusp-trap are shown in table 2.1, fig. 2.8 and in fig. 2.9 . The positron beam-line, marked with the red arrow in fig. 2.9, transports particles from the positron source to the Cusp-trap and is encased in solenoid coils marked red in fig. 2.9.

As positrons are light particles, the magnetic field necessary for their transport is not very strong. Therefore moving them around the corners of the beam-line can be facilitated by the fields generated by the solenoid coils and transport coils along their way. The coils from table 2.1 are also used to further focus the antiproton beam. For heavier particles the required magnetic force is however considerably higher and therefore a purely magnetic transport around corners would not be feasible because of the required currents. In fig. 2.8 a photograph depicting the six-way cross at the junction of the positron beam-line, MUSASHI and the Cusp-trap is shown.

Table 2.1.: Specifications and dimensions of the coils of the transport line from MUSASHI to the Cusp-trap summmarized, data from [27]. Position of the coils measured from the center of MUSASHI's MRE to the outer edge of the coil.

name	inner radius [mm]	outer radius [mm]	length [mm]	turns	position on z [mm]
coil A	125	153	150	150	1311
coil B	200	204	96	48	1831
coil C	125	180	30	147	2041

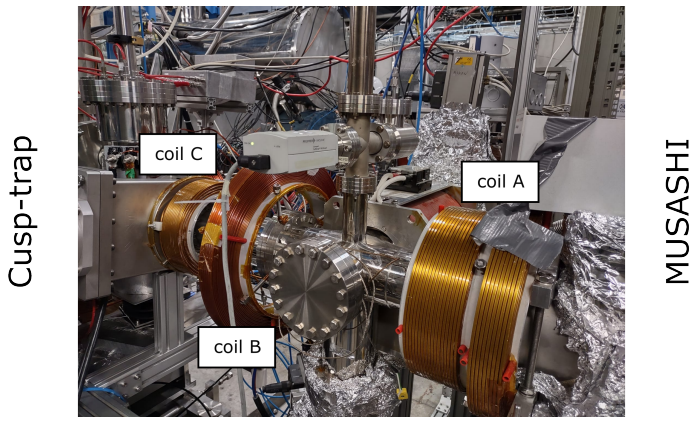

Figure 2.8.: Photograph of the current coil setup around the six-way cross between MUSASHI and the Cusp-trap.

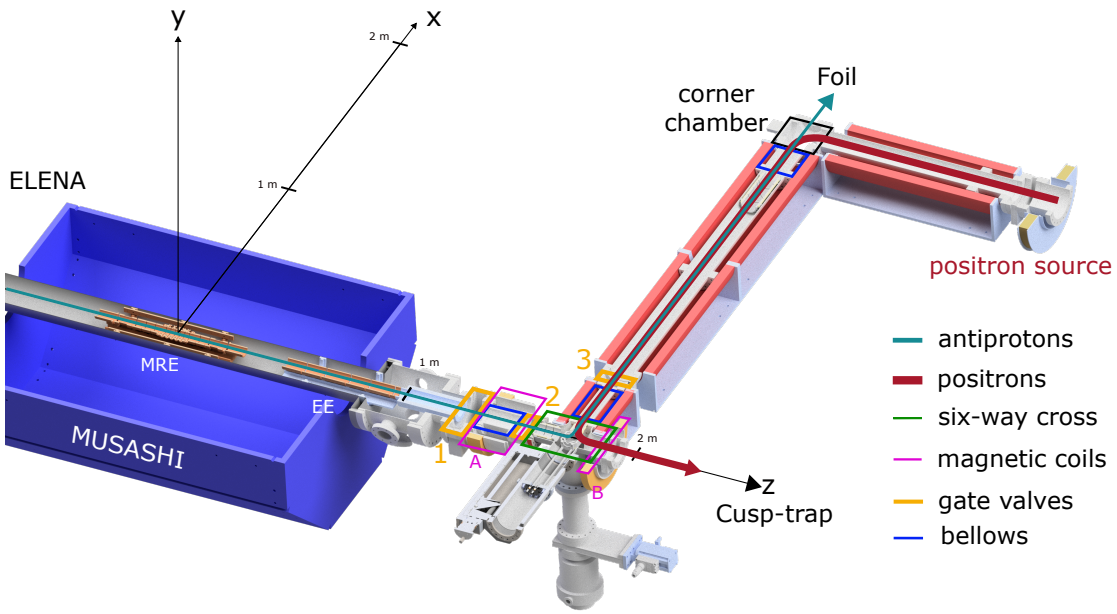

Figure 2.9.: Cross-sectional view of the positron beam-line with MUSASHI depicting the path of the particles. The gate valves (GV) (orange) are numbered, and the coils are marked according to the conventions from table 2.1.

3. Charged particle motion in $\vec{E}$ & $\vec{B}$ fields

This chapter gives a review of basic electrodynamics, followed by methods used in SIMION for charged particle trajectories.

3.1. Maxwell Equations

To be able to make predictions about the behavior of charged particles in electromagnetic fields, a basic understanding of these fields is necessary. In vacuum the vectorfunctions $\vec{E}(\vec{R},t)$, for the electric field, and $\vec{B}(\vec{R},t)$, the magnetic flux density, with $\vec{R}$ as the radius vector and t as time, provide enough information to describe electromagnetic fields [28].

With these two vectorfunctions the Maxwell equations can be formulated such that:

$$\vec{\nabla} \cdot \vec{E} = \rho/\epsilon_0 \tag{3.1}$$

$$\vec{\nabla} \times \vec{E} = -\frac{\partial \vec{B}}{\partial t} \tag{3.2}$$

$$\vec{\nabla} \cdot \vec{B} = 0 \tag{3.3}$$

$$\vec{\nabla} \times \vec{B} = \frac{1}{c^2}\frac{\partial \vec{E}}{\partial t} + \mu_0 \vec{J} \tag{3.4}$$

In these equations ϵ_0 is the permittivity of free space, μ_0 is the permeability of free space, c is the speed of light, $\rho(\vec{R},t)$ is the charge density, and $\vec{J}(\vec{R},t)$ is the total current density. By introducing a scalar potential u and a vector potential $\vec{A}$ with the relationships:

$$\vec{E} = -\vec{\nabla}u - \frac{\partial \vec{A}}{\partial t} \tag{3.5}$$

$$\vec{B} = -\vec{\nabla} \times \vec{A} \tag{3.6}$$

for the case that the charges q_i, currents, and fields do not change with time, eq. (3.2) and eq. (3.4) are simplified to:

$$\vec{\nabla} \times \vec{E} = 0 \tag{3.7}$$

$$\vec{\nabla} \times B = \mu_0 \vec{J} \tag{3.8}$$

This leads to the electric field being defined solely by eq. (3.1) and eq. (3.7), while the magnetic field is defined only by eq. (3.3) and eq. (3.8). This independence of electricity and magnetism leads to electric fields being only defined by the scalar potential u:

$$\vec{E} = \vec{\nabla} u \tag{3.9}$$

By plugging this expression into eq. (3.1) the Poisson equation is obtained:

$$\vec{\nabla} \cdot \vec{\nabla} u = -\rho/\epsilon_0 \tag{3.10}$$

Here ρ and u are now both functions of space. If one now assumes no space charge with $\rho = 0$ throughout the defined volume, excluding boundary surfaces, a special case of the Poisson equation, the Laplace equation is found:

$$\vec{\nabla} \cdot \vec{E} = 0 \tag{3.11}$$

3.2. Electrostatic Force and Acceleration

Coulomb's law defines the force acting between two charged particles, or multiple charged particles:

$$F_e = \frac{1}{4\pi\epsilon_0} \frac{q_i q}{r^2} \tag{3.12}$$

$$F_e = q_i \sum_n \frac{q_n}{4\pi\epsilon_0 r_n^2} \tag{3.13}$$

where q_i is the particle's charge. The electric field can be interpreted as the force per charge. It is also possible to look at it in the sense of change in work in relation to charge over distance, which gives us for the electric field density:

$$E = \frac{F_e}{q_i} = \frac{d(W/q_i)}{dr} \tag{3.14}$$

If we see the electric field as the generator of the force on the charged particle, and the force as the cause for acceleration we arrive at [29]:

$$F_e = -q_i E \tag{3.15}$$

$$a = F/m = dv/dt = -(q_i E)/m \tag{3.16}$$

3.3. Transport in a magnetic field

Solenoids are electromagnets used for the production of homogeneous magnetic fields. As charged particles experience a force when moving through a magnetic field, they can cause acceleration and ultimately influence the direction these travel in. Charged particles follow magnetic field lines. How strongly they are influenced can be deduced with the Lorentz force:

$$F = q\vec{E} + q(\vec{v} \times \vec{B}) \tag{3.17}$$

By only looking at the magnetic component of the force (or assuming no electric field) one can arrive at the conclusion, that the relation between the particle's charge q and its mass m is the defining factor for how strongly it is influenced by the magnetic field.

$$F = ma = q(\vec{v} \times \vec{B}) \tag{3.18}$$

$$a = \frac{q}{m}(\vec{v} \times \vec{B}) \tag{3.19}$$

As solenoids consist of helically bent wires, through which a current is conducted, the resulting magnetic field $\vec{B}$ can be calculated using the Biot-Savart law:

$$\vec{B} = \frac{\mu_0}{4\pi} \int \frac{I \mathrm{d}\vec{l} \times \vec{r}}{|r|^3} \tag{3.20}$$

In this the infinitesimal length and direction of a section of the wire is $\mathrm{d}\vec{l}$, I is the amount of current in that section, and $\vec{r}$ is the displacement vector from the section of wire current to the point where $\vec{B}$ is measured [30].

If we assume that particles traveling through the solenoid have a constant E_{kin} that is limited to the $\vec{v} = (0, 0, v_{z0})$ component of their movement we can anticipate the trajectories the particles take through the solenoid. In each xy-plane they traverse, there is a homogeneous magnetic field, that applies a Lorentz force from eq. (3.17) to the particles. As in this case $\vec{B}$ only has a z-component, and $\vec{v}$ and $\vec{B}$ are constant, this force always stays in the xy-plane and acts perpendicular to the motion of the particle caused by v_{z0}. It behaves as a centripetal force, causing uniform circular motion. The radius of this circular motion is therefore defined by

$$\vec{R} = v_{0\perp}/\omega_C = m v_{0\perp}/(|q|B_z) \tag{3.21}$$

where $v_{0\perp}$ is the velocity of the particle perpendicular to the xy-plane, ω_C is the cyclotron frequency, m is the mass and q is the charge of the particle [31]. Together with the initial movement of the particle this results in a spiral shaped trajectory [32]. An example of such a magnetic field and the trajectories caused by it can be found in fig. 3.1.

3.4. Magnetic Focusing

By adjusting the field of the coil in such a way, that one can choose at which position in the circular movement the particles leave the magnetic field, it is possible to focus the particles after the coil. After passing the distance

$$h = v_{z0} T \tag{3.22}$$

where

$$T = 2\pi/\omega_C \tag{3.23}$$

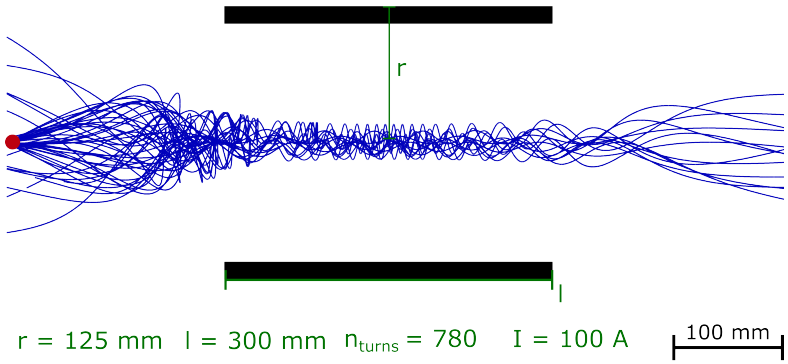

Figure 3.1.: Slice through a solenoid magnet (black), revealing the trajectories of a 250 eV antiproton beam (blue) from a point source (red). Some of the particles get deflected back because of their angle being too steep. The magnetic field of this solenoid was calculated using the Biot-Savart law in SIMION. The produced field exhibits 2500 G in the center of the magnet.

is the time required to finish a full revolution, the particles return to the same field line that they started from. By choosing the parameters, e.g. the current for the coil accordingly, one can let the particles leave the magnetic field while they are still being accelerated towards the center of the field. An example for this is given in fig. 3.2, where the shown coil shares its specifications and settings with coil C from fig. 2.9. This coil is used to further focus the particles entering the Cusp-trap.

3.5. The SIMION Method for solving charged particle transport in $\vec{E}$ & $\vec{B}$ fields

SIMION is an ion optics simulation software that solves the Laplace equations to calculate the electrostatic field within a potential array (PA) which can include a number of electrodes. While fields and their effects on ions are limited to the arrays, the motion of particles is not. As the computational requirements increase with the number of points making up a PA, multiple PAs can be used in a simulation to reduce required memory by omitting field free spaces. Here only a short overview of the functions and the processes used for the following simulations are given. This section is based on SIMION's supplemental documentation and its user manual [29, 30].

3.5.1. Relaxation Method and PAs

The way fields are calculated is by first defining a geometry inside of the PA. This is done by assigning each point, also called a graphical unit (GU), in the array an 'electrode' with a defined potential or a 'non-electrode' attribute based either on SIMION's proprietary

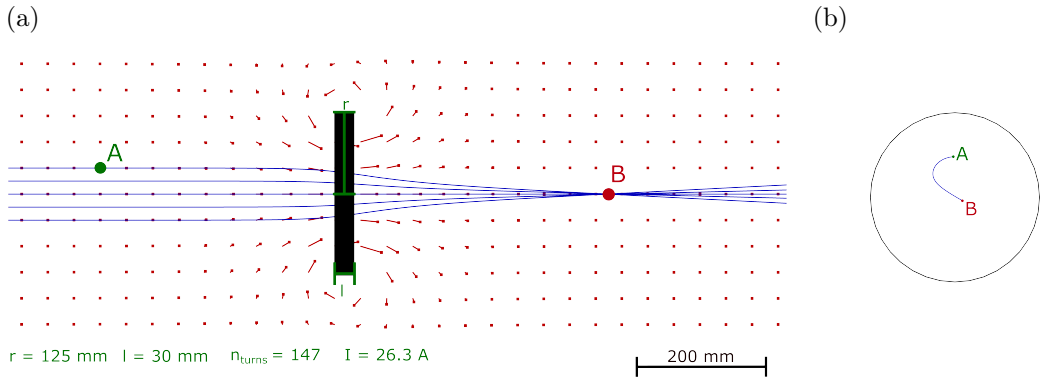

Figure 3.2.: (a) Side view of particle paths (blue) for a parallel beam through the field, depicted by vectors (red), generated by a focusing coil (black) to focus the beam. (b) Frontal view of the trajectory of one particle through a coil set to focus. The particle does not finish a full revolution of the cyclotron motion from entering the field (point A) until leaving the field and therefore is accelerated towards the center at the end (point B).

'.gem' files, the import of CAD files or by simply using the graphical user interface (GUI). The relaxation method, a finite difference method, is used to calculate the value for each point in the PA. The nearest neighbors of each point are used to calculate the value of the center point. This is done by using the average:

$$2D: \; P_{0\ new} = (P_1 + P_2 + P_3 + P_4)/4 \tag{3.24}$$

or

$$3D: \; P_{0\ new} = (P_1 + P_2 + P_3 + P_4 + P_5 + P_6)/6 \tag{3.25}$$

respectively for 2D or 3D PAs. By repeatedly averaging the values for all of the non-electrode points in the PA, ultimately the value for each point starts converging. This process is repeated until a predefined convergence limit is reached.

Dirichlet and Neumann Boundary Conditions

The aforementioned process relies on finding solutions based on fixed boundary conditions. The Dirichlet boundary conditions dictate that the solution of the Laplace equation is determined if a voltage is specified for a boundary surface. The Neumann boundary conditions can also provide a unique solution by defining the normal derivative of the potential on a boundary. For a boundary S that can be subdivided into $S = S_1 + S_2$ follows:

$$\nabla^2 V(\vec{r}) = 0 \qquad \vec{r} \in \Omega \tag{3.26}$$

$$V(\vec{r}) = f(\vec{r}) \qquad \vec{r} \in S_1 \tag{3.27}$$

$$\frac{\partial V(\vec{r})}{\partial n}(\vec{r}) = g(\vec{r}) \qquad \vec{r} \in S_2 \tag{3.28}$$

where $\frac{\partial V}{\partial n}$ is the normal derivative, pointing outside, V is the electric potential of the volume, Ω and f are the potentials on the boundary S. At a given boundary only one of the two boundary conditions can be used. So in the case above S_1 is defined by a Dirichlet and S_2 by a Neumann boundary condition. SIMION finds the solutions by refining the potentials from the points defined as electrodes in the PA, which represent the Dirichlet conditions, to the edges of the PA, which are defined by Neumann conditions. Mirrorplanes are also defined as Neumann conditions [33]. The effect that defining the edges of a PA differently can have on a calculated field can be seen in figure 3.3.

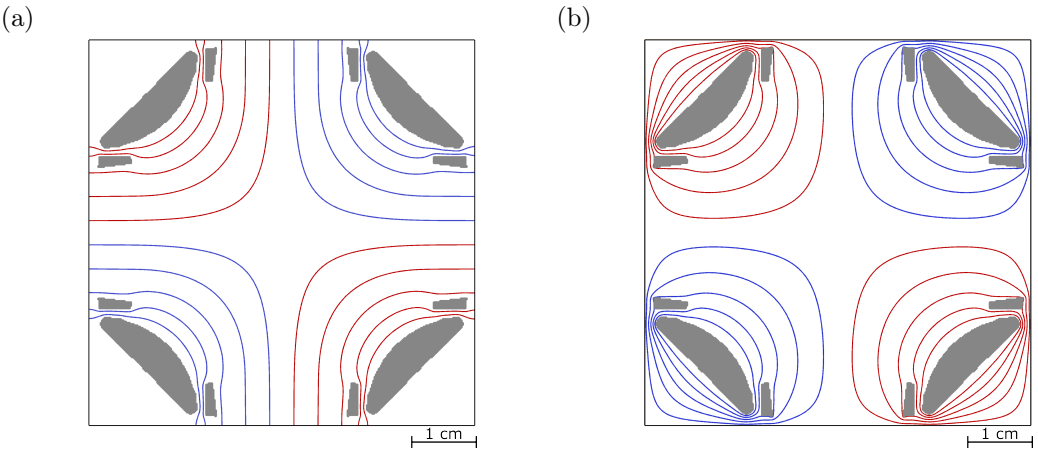

Figure 3.3.: Contour plots of the same electrodes set to identical potentials. Defining the surrounding edges of the PA either as (a) zero Neumann-conditions, or (b) as zero Dirichlet-conditions, has an impact on the calculated field. The black boxes around the electrodes are 60 × 60 mm^2 and represent the lines on which the boundary conditions are defined.

For fig. 3.3(a) at the edges of the simulated array the potential falls off abruptly. A particle entering or leaving the defined space at one of these positions has its E_{kin} calculation affected, falsifying the results of following trajectory calculations. If the simulated space however is defined with Dirichlet conditions, like in fig. 3.3(b), the potential can be chosen to reach predefined values at these boundaries. This, however, can also be a misrepresentation of the electric fields if the distance is too short and the gradient is therefore too steep in the simulation. To ensure that trajectory calculations do not get negatively impacted by the boundary conditions, the size of the arrays and the trajectories the particles will take trough them have to be considered when simulating electrodes.

4. Design of the beamline

In this chapter the process of simulating and designing the electrostatic parts necessary for the $\overline{p}$ transport from MUSASHI to the target are discussed. In order to obtain reliable predictions, the quality and shape of the $\overline{p}$ beam from MUSASHI was studied. The SIMION software package was used for the simulation and tracking of the trajectories of the particles exiting the MUSASHI trap, after which different designs for the bending apparatus were tested with the simulation of the trap. For a systematic optimization of the design 'workbench user programs' in the form of lua code were used, that automatically searched for the optimal geometry and the corresponding potentials for the electrostatic quadrupole bender. To sufficiently improve transmission and decrease beam spot size, additional electrostatic lenses were included in the design.

MUSASHI is estimated to trap more than 1×10^6 $\overline{p}$ from each shot from ELENA. In the previous beam campaign for annihilation studies, with a different configuration of the experiment, only about 1×10^3 to 2×10^3 particles were detected for each AD-cycle, where 20 s was the duration of one slow extraction from MUSASHI [34, 35].
As the measurements were done at a position behind the Cusp-trap, moving the set-up for the annihilation studies closer to the exit of MUSASHI is expected to increase the number of $\overline{p}$ transmitted to the target. Off-axis particles are especially affected by the magnetic cusps of the trap and are expected to be more efficiently transported to a new target position, omitting the Cusp-field. The aim of this thesis is to improve upon the number of antiprotons transmitted to the target, as with the new Timepix4 detectors [15] a higher readout rate is possible, and to ultimately relocate the annihilation experiment to the end of the positron beam-line (as seen in fig. 2.3 where the position of the foil is marked) in order to avoid vacuum interruptions when switching between antihydrogen production and slow extraction experiments. To make use of the beam when the main experiment is not taking data (e.g. maintenance reasons), the parts of the bending apparatus, that could negatively impact the antihydrogen production, are made to be retractable. The quadrupole deflector, which due to its shape could block parts of the $\overline{p}$-beam for the main experiment, and an Einzel lens with a small diameter, i.e. the one on the side of the positron beam-line, were designed with the necessary tolerances in mind.

4.1. Slow $\overline{p}$ Extraction

The shape of the beam currently produced by MUSASHI [24] was further investigated. Changes in the ASACUSA apparatus' settings were incorporated to improve and optimize the beam for bending. The simulation includes the MUSASHI electrodes, its solenoid

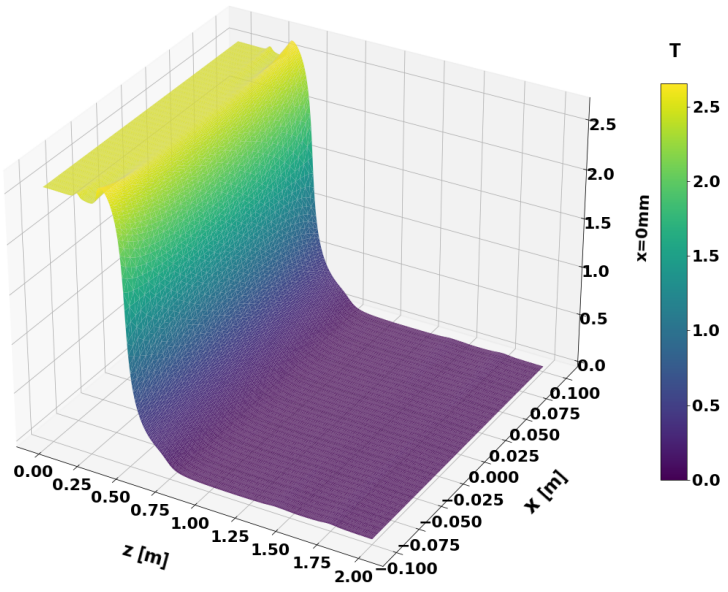

Figure 4.1.: Plot of the cylinder-symmetrical field map for MUSASHI's B-field in the zx-plane.

and the transport coils along the beam-line.

For the electrostatic PA the electrodes of the MRE and of the EE were modeled according to the dimensions in section 2.4, fig. 2.6 and implemented in an array with cylindrical symmetry. For the simulation, a resolution of 0.3 $\frac{GU}{\text{mm}}$ was used. This means that every mm was represented by about 3.3 points in the simulation. MUSASHI's solenoid B-field was imported from a field map. The B-field of the transport coils was added to the simulation with Lua code using the "simionx.MField" module. The map shown in fig. 4.1 was calculated with TRICOMP (an older FEM solver). For its implementation in the simulation the "simionx.FieldArray" module was used. Fig. 4.2 shows different plots of the electric and magnetic field used in the simulated space respectively. The position and settings of the coils correspond to their standard configuration, as seen in table 2.1.

From assessments depicted in fig. 4.3 it is apparent, that small changes in the initial size of the particle distribution in the MRE can produce large differences in beam diameter in the extracted beam at a location downstream. The current standard settings of MUSASHI provide a strongly compressed center for the $\overline{\text{p}}$ cloud, containing 60% of the particles, and a thin spread out halo component around it, with an estimated radius size of 0.4 and 4 mm respectively. The blue trajectories in fig. 4.3 start with a radius of 1 mm, yellow with a 0.5 mm and green is set to a radius of 0.25 mm at the center of the MRE. The lowest

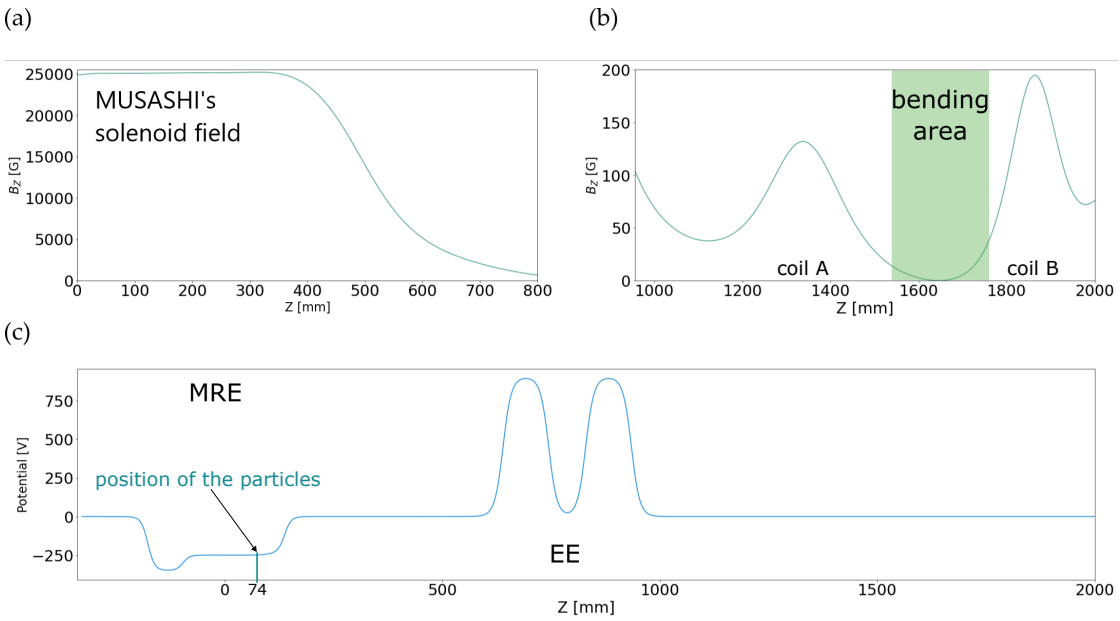

Figure 4.2.: (a) Plot of the the field B_z acting on a particle traveling through the PA on the z-axis in MUSASHI. (b) Plot of B_z acting on a particle along the transport line from MUSASHI towards the Cusp-trap. (c) Plot of the electrical potential on the z-axis from MUSASHI's center point to the Cusp-trap.

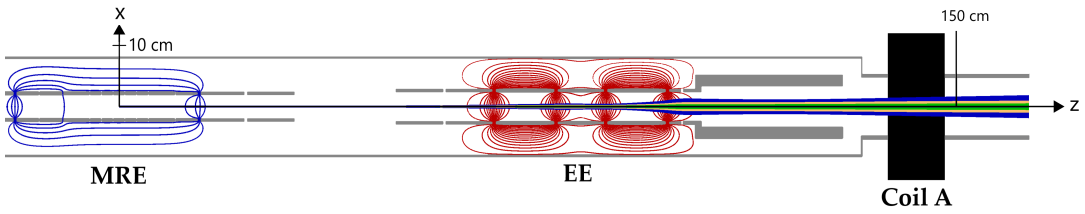

Figure 4.3.: Cross-section of the cylinder symmetrically electrodes from MUSASHI with example beams starting with different radial expansions in the MRE. The blue lines belong to particles starting with a radius of 1 mm, yellow with a 0.5 mm, and green with a radius of 0.25 mm. The contours in red represent positive potentials and the ones in blue negative potentials. A small change in the starting radius can change the final radial expansion of the beam significantly.

Table 4.1.: Result of a simulation starting with a 0.5 mm wide center part of the plasma (z = 1515mm).

	average value	Standard deviation σ	unit
x	0.01	2.73	mm
y	−0.03	2.77	mm
v_x	0	0.74	mm/µs
v_y	0	0.74	mm/µs
E_{kin}	250.32	0.57	eV

potential in the MRE is at the position of the UCE on the left side at −350 V and the highest at of the EE at 905 V. The voltages are chosen to represent the current standard settings of the slow extraction procedure, according to the explanation given in section 2.4.

To represent the plasma during the extraction, the particles were created in a filled flat circle with homogeneous distribution in the xy-plane. As mentioned in section 2.4, the transverse kinetic energy of the particles inside the potential well is being controlled by the cooling and the potential of the electrodes [24] during extraction. To mimic this, the particles were given a uniform kinetic energy distribution between 0 and 2 eV pointing 90° away from the z-axis in the direction of radial expansion.

By comparing the results of [24] and [36] with this simulation, it was decided to focus the optimization on an initial plasma radius of 0.25 mm and to superimpose another distribution with a 2.5 mm radius inside of the MRE's potential, as this combination, seen in fig. 4.4, provided similar results to the ones reported in [24, 36]. To speed up simulation time, the path of the particles was shortened by moving them 74 mm downstream along the z-axis, still inside of the flat part of the well potential (see fig. 4.2). This reduced the running time significantly without affecting the spread, shape or the energy of the particles. The results of this simulation can be seen in fig. 4.4 and in fig. 4.5. For the center part the important metrics can be found in table 4.1. For this simulation 10^5 particles were used for each of the halo and the center part of the plasma. While the center part had a transmission of 100% to the depicted test plane, only 45.72 % of the halo was transmitted out of the apparatus.

As the beams radial expansion greatly increases after leaving the field of MUSASHI's solenoid and passing through its stray fields, a first Einzel lens is necessary before the quadrupole deflector to focus the beam for the bending and another lens is necessary to correct the deflection of the particles caused by their transverse motion in the magnetic field (e.g. field of the transport coils).

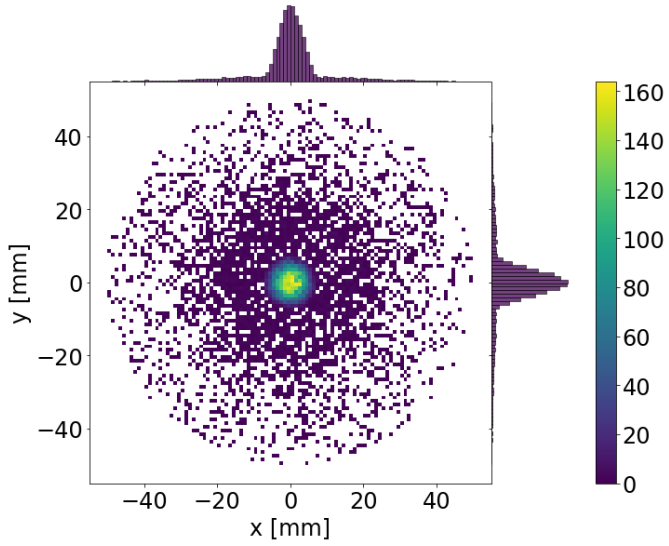

Figure 4.4.: Beam-profile taken at z = 1515 mm, at gate valve 2 from fig. 2.9, with the results of 2×10^5 particles extracted from MUSASHI, providing the initial beam necessary for the optimization of the bending setup.

4.2. Quadrupole deflector

An electrostatic quadrupole deflector was chosen as the means for bending the beam towards the new position of the target foil. It changes the trajectory of charged particles passing through it and deflects them depending on the polarity of their charge and their momentum. This can be used to deflect a beam into a desired direction or be put to use in a mass spectrometer by using its energy dispersive properties [37]. This kind of deflectors consists of at least four, typically cylindrical electrodes, most commonly referred to as rod electrodes, that are arranged in a square. Two electrodes are then held on the same potential and the remaining two electrodes set on a different potential. Depending on the application and the kinetic energy of the particles, the second set of electrodes can be set to the opposite polarity. The resulting field varies in strength depending on the distance to the electrodes. Therefore the force applied to the particle is dependent on the particle's position and can be calculated with the potential:

$$V = K(x_1^2 - y_1^2) + V_0 \tag{4.1}$$

where K is a constant for a particular deflecting field and V_0 is a constant potential for a particular ion that traverses the field. The position of the particle is defined by the coordinates x_1 and y_1, fixed by the diagonals of the quadrupole field, as seen in fig. 4.6 [38]. The direction the particles are deflected towards is dependent on their charge, momentum, and the potential energy (PE) required to traverse the electrostatic field. In fig. 4.6 an example of a simple quadrupole deflector is shown. The $\overline{\text{p}}$ are bent by the electrostatic field created by four circular rod electrodes set to potentials of opposite polarity. Depending

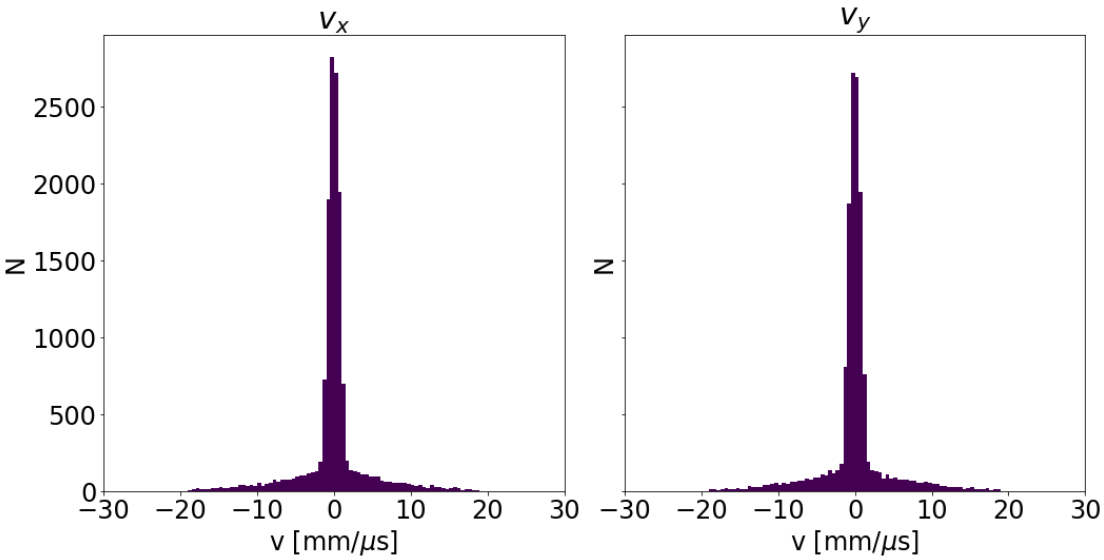

Figure 4.5.: Histograms depicting the velocities in x- and y-direction for the beam at z = 1515 mm.

on the potentials chosen for the electrodes, particles can be accelerated or decelerated inside of the deflector. However, after leaving the quadrupole, the energy returns to its initial value.

For the quadrupole deflector the first step was to test existing designs, like the ones described in [37] and [38], by adapting them in size and then using them with the beam shown in fig. 4.4. As the delfector does not exhibit the same symmetries as MUSASHI, it was added to the simulation in a separate planar array. All three designs were scaled to the same outer dimensions, fitting in the existing six-way cross shown in fig. 2.9. This shielding houses the electrodes and reduces the effects of outside influences on the quadrupole field as seen in the example depicted in fig. 4.7 where the Einzel lens, marked as E1, slightly affects the field at the opening of the quadrupole deflector. The middle rings of the Einzel lenses depicted there are kept on a potential, while the other two rings are set to ground. As these ground rings are too short [39] they can not stop the formation of fringe fields at the entrance of the deflector, as there is not enough space for the potential to completely return to ground between the two parts. Without shielding around the deflector this effect would be more pronounced, ultimately moving the beam off axis before entering, thereby reducing its overall efficiency and annihilating the $\overline{\text{p}}$ on one of the electrodes.

To determine which of the designs would be best suited for our application a 5 mm wide beam consisting of 10 equidistantly distributed antiprotons with an energy of 250 eV was bent by manually adjusting the voltages of the electrodes until it was possible to bend all particles. To take fringe fields on the outside of the deflector into account, the beam was directed towards the input aperture of the deflector from 5 cm away. The outer

(a) (b)

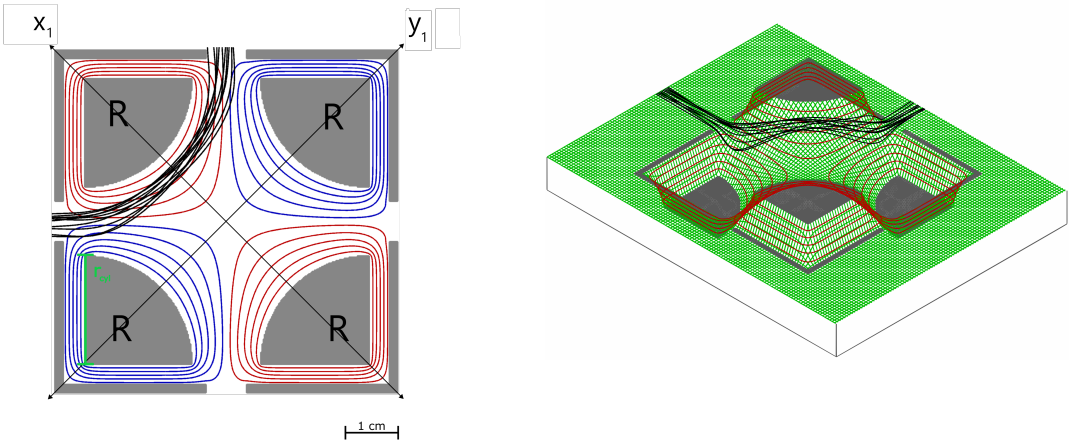

Figure 4.6.: (a) A crossectional view of an electrostatic quadrupole is depicted. The blue contours show the negative potential and the red ones indicate the shape of the positive potential. The rod electrodes are marked with (R) and their radius is marked in one (green). (b) The corresponding PE view for the antiprotons in a quadrupole field is shown. The difference in potentials creates an electrostatic field of saddle shape. The antiprotons are attracted towards the positive potential and repulsed by the negative ones.

dimensions of the quadrupole deflector's shielding was cube shaped with a width of 65 mm and reused for all tests. All simulations of the quadrupole deflector in this section were set to $480 \times 480 \times 480$ GU resulting in resolution of 0.14 $\frac{GU}{mm}$.

Even though bending is possible with circular rod electrodes alone, as shown in fig. 4.8, this is not the optimal approach because of the field expanding to the outside of the housing. In part this can be mitigated by the housing, as already discussed in a previous paragraph (fig. 4.7). To further reduce the number of particles entering the actual quadrupole off-center, this issue can be addressed by trying to control the field at the entrance apertures of the housing using additional electrodes. These so called shims (marked A for entrance apertures in fig. 4.9) are two rectangular electrodes on either side of the apertures that extend 4 mm into the deflector. For the purpose of these simulations they were kept to a thickness of 1 GU. To reduce the fringe fields at the entrance for the entering particles these can be set to the same potential, halfway between the voltages of the two rod electrodes [37].

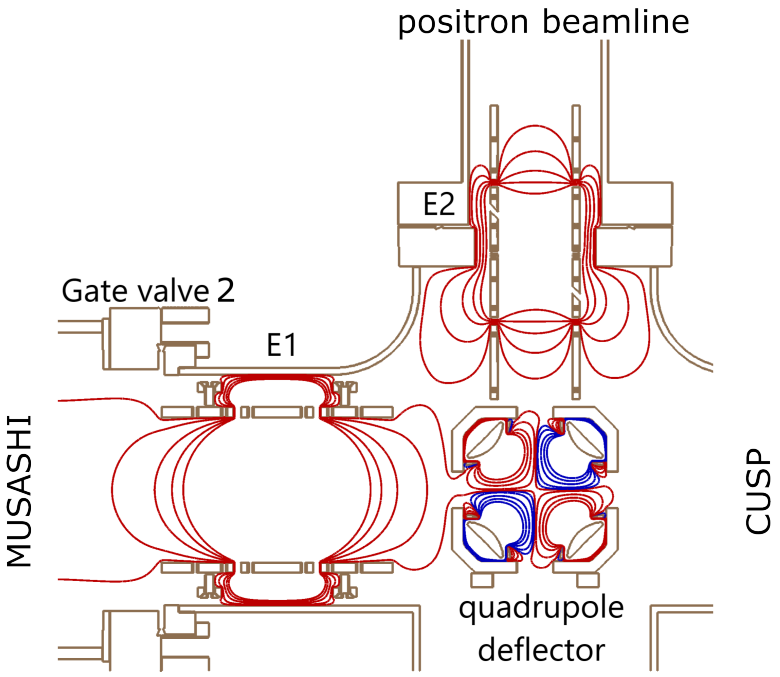

Figure 4.7.: Cross-section of a PA showing the bending elements. PE contours shown are 5V, 25 V and from there on in 50 V steps up to 175 V. The blue contour lines are the same values, but with negative potentials.

(a)

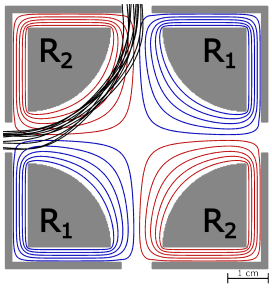

(b)

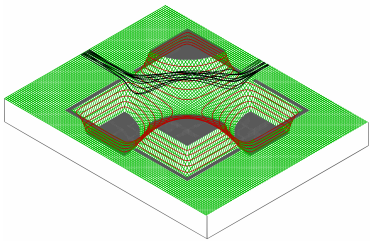

Figure 4.8.: (a) The center slices for quadrupole deflector with the rod electrodes $P_{R_1} = -200$ V and $P_{R_2} = 200$ V is shown. [30]. Contours in red depict positive potentials, blue negative potentials, black the trajectories of antiprotons and gray the electrodes. (b) A plot of the corresponding potential energy (PE) view for the antiprotons is depicted.

As the field created by circular electrodes does not produce the optimal hyperbolic field shape, aberrations are introduced with this kind of deflectors. Their efficiency can be

(a) (b)

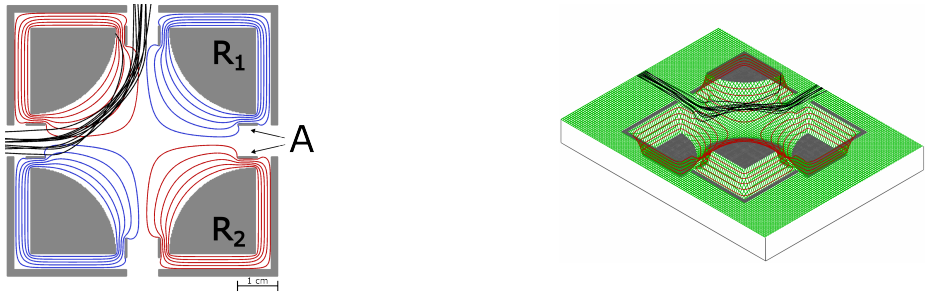

Figure 4.9.: (a) The center slices for quadrupole deflector with rod electrodes $P_{R_1} = -320$ V and $P_{R_2} = 280$ V and entrance apertures $P_A = -20$ V [37]. Contours in red depict positive potentials, blue negative potentials, black the trajectories of antiprotons and gray the electrodes. On the right side the corresponding potential energy (PE) view for the antiprotons is depicted.

increased by closer approximating the electrostatic field of the quadrupole to the optimal hyperbolic flight-path of the particles. One way this can be achieved is by machining the electrodes to resemble hyperboles on the sides facing the particles. The increased cost for the production of these more elaborate shapes, however, offsets their benefit. A similar increase in efficiency can be achieved by using two shims (marked as S_1 and S_2 respectively in fig. 4.10) on both sides of the opening and setting them to different potentials between P_{R_1} and P_{R_2} as opposed to the previous case where they are set to same potentials (marked A). This can be seen in fig. 4.10 [38]. For this purpose the same geometry as in fig. 4.9 was used and only the voltages were adjusted.

(a) (b)

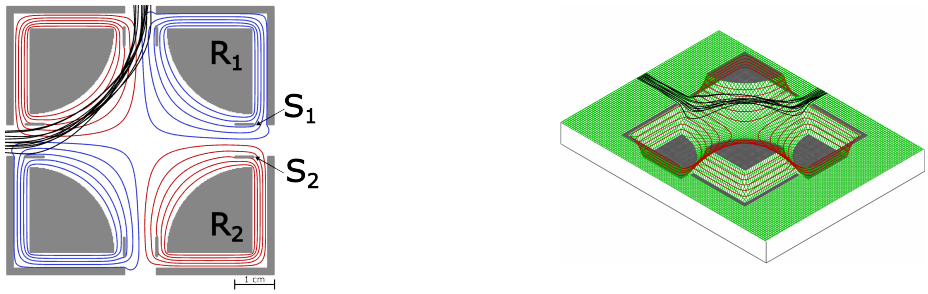

Figure 4.10.: (a) The center slices for quadrupole deflector with rod electrodes $P_{R_1} = -180$ V and $P_{R_2} = 180$ V and shims $P_{S_1} = -90$ V and $P_{S_2} = 90$ V [37]. Contours in red depict positive potentials, blue negative potentials, black the trajectories of antiprotons and gray the electrodes. On the right side the corresponding potential energy (PE) view for the antiprotons is depicted.

4.3. Geometry Optimization

The position of the bending apparatus inside of the six-way cross, (fig. 4.11), between the MUSASHI trap and the Cusp-trap sets the limitations in size and shape for its design. Inside the cross, the maximum width of a cube shaped deflector is dictated by the a 100 mm diameter pipe used for installation, storage, and actuation of the quadrupole and its manipulator. After subtracting tolerances for the moving mechanism, the space needed for mounts and electrical connections the housing of the deflector is left with about 65 mm maximum width for its outer dimensions. Reducing the size of the deflector impacts its bending capabilities and subsequently the transmission, negatively. However, moving the deflector in and out of the beam through the port marked as "manipulator" in fig. 4.11 is necessary to be able to switch between the $\overline{\mathrm{H}}$ and annihilation experiment without braking the vacuum.

To increase the number of particles deflected by the bender and transmitted to the target, steering Einzel lenses will be placed before and after the quadrupole deflector. Additionally a third Einzel lens will be placed in front of the target, to reduce the beam spot size. The parts used in this work will henceforth be referred to as (see fig. 4.7):

- qaudrupole deflector
- Einzel lens 1 (E1), situated before the deflector on the MUSASHI side for the best possible steering of the beam entering into the deflector.
- Einzel lens 2 (E2), a smaller diameter Sikler-type einzel lens used to steer the particles after bending them through the field of the transport coils. Retractable and connected to the deflector so as to not limit the number of positrons for the main experiment.
- Einzel lens 3 (E3), also a Sikler-type lens used for minimizing the beam spot size on the target foil. E3 is located in the positron beam line and not visible in fig. 4.7.

4.3.1. Electrode dimensions of the quadrupole deflector

To reduce the effect of fringe fields on the qudrupole field to a minimum (as mentioned in section 4.2 and fig. 4.7) a housing for the electrodes was necessary. This also doubles as a mount for the deflector and accommodates the mounting plate for the actuator and the electrical connections. As the beam after MUSASHI from fig. 4.4 becomes wider at the position of the bender than the diameter of the opening in the housing, changes to the set-up were necessary.

One way of limiting the beam expansion and preventing particles annihilating on the housing of the deflector is using an Einzel lens. By focusing the beam before entering the housing the number of particles entering the deflector can be increased. However, the space between the quadrupole deflector and the gate valve 2 (fig. 2.9), placed at the port

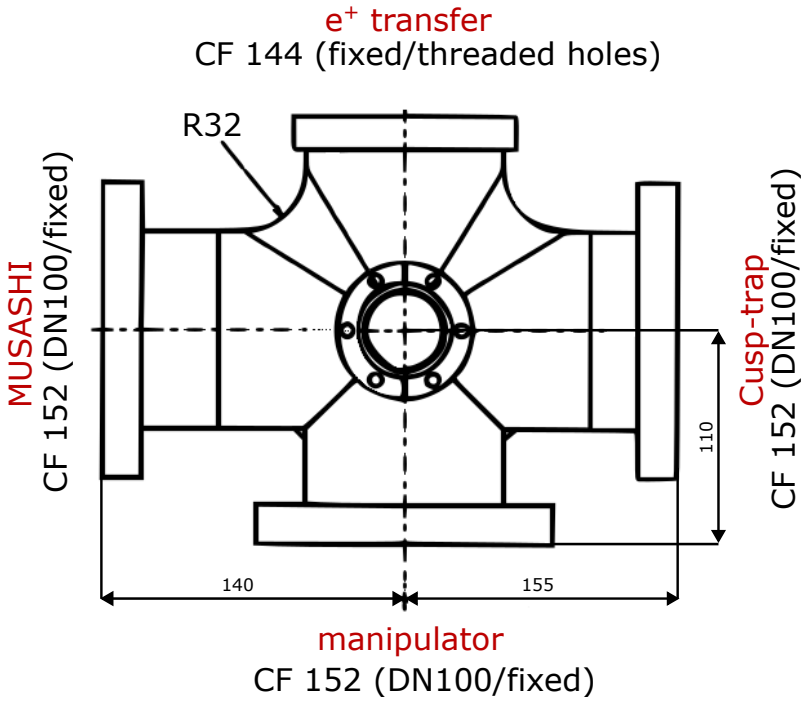

Figure 4.11.: Schematics of the custom made cross between MUSASHI, the Cusp-trap and the positron beamline. Its dimensions are limiting the size of the quardrupole deflector and the length of the Einzel lenses.

marked as "MUSASHI" in fig. 4.11, limits the length of an Einzel lens. Short lenses are prone to introducing aberrations to beams, which would make them harder to control. By moving the focal point of the Einzel lens close to the entrance of the deflector most particles would be able to enter, but the divergence after the focal point would hinder them from leaving the deflector, or would require significantly higher voltages. An optimization of the geometry, with respect to the design chosen in the previous section, was performed to increase its efficiency specifically for the the beam produced by MUSASHI.

This optimization process changed:

- the radius r_{cyl} (as marked in fig. 4.6) of the corner electrodes, machined by quartering a rod,
- the position of the shims, keeping the space between them and the rods constant,
- the size of the openings in the shielding.

By multiplying the variables defining the dimensions of these parts by a factor, the shape of the deflector in the PA could be changed. The corners of the shielding were fixed

coordinates, as these were the points from which the circular rod electrodes were defined and the other distances were based on. By reducing r_{cyl} of the rod electrodes, without changing their respective positions in the corner of the housing, and moving the shims to maintain the proportionally same distance to the rod electrodes, the available space for the openings in the housing was increased. A fully parameterized geometry file was used to have the dimensions of the electrodes adjusted by a Lua code. The loop adjusted different variables that defined the geometry by multiplying them by a factor. It then updated the geometry based on the resulting new dimensions step by step, refined the changed array, and evaluated the beam after each iteration. To keep the results of each step of the geometry sweep comparable [40], the potentials were optimized using a simplex optimizer for each geometry.

To include the effect of Einzel lenses on the performance of each geometry, they were also incorporated in the PA. Although these were Einzel lenses with split electrodes and a Sikler-type Einzel lens (further explained in section 4.3.2), all segments of their middle rings were set to one potential. The simplex optimizer was optimizing the potentials of E1, the two pairs of rod electrodes of the bender and the two sets of shims with one variable each. E2 was set to a fixed voltage, as the test plane, at which the beam was evaluated, was between it and the deflector. For each optimization run the same beam consisting of 100 randomly chosen particles from fig. 4.4 was used. By changing the geometry as described above, the diameter of the opening could be increased to more than double its original size. With two Einzel lenses a transmission of 100% was achieved for the center part of the beam for the geometries adjusted by a factor of 0.8 or lower.

Table 4.2.: Voltages and results for f_{metric} for the different geometries in dependence of the shrinking factor for r_{cyl}.

shrinking factor	f_{metric}	P_{R_1}[V]	P_{R_2}[V]	P_{S_1}[V]	P_{S_2}[V]	P_{E1} [V]
1.0	6417.02	−216.19	305.90	−98.37	58.36	12.72
0.9	2101.84	−137.22	862.63	−138.26	277.36	−213.13
0.8	66.98	−251.91	675.28	−281.79	349.74	−249.72
0.7	67.62	−357.57	859.97	−389.62	360.84	−206.93
0.6	67.25	−300.86	2481.48	−674.75	−65.96	−189.30
0.5	69.77	−901.93	1051.27	−511.89	570.70	−252.60

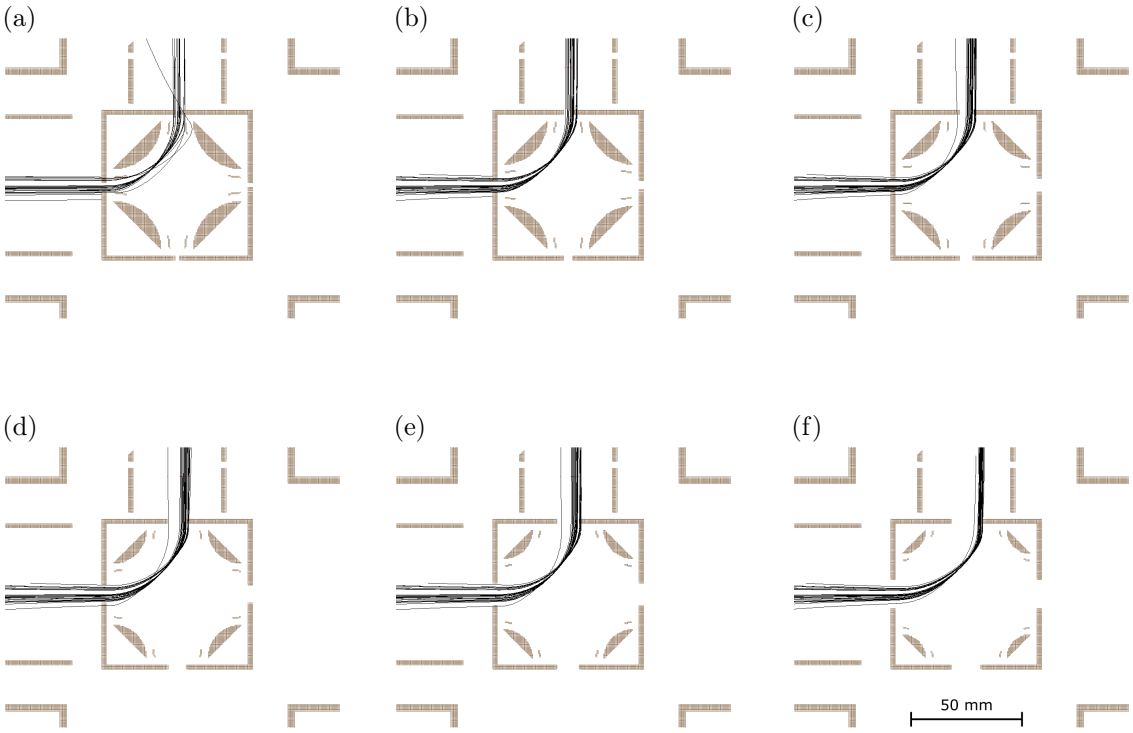

Figure 4.12.: A selection of screenshots taken during the geometry sweep performed on the proportions of the quadrupole bender. While (a) $1 \times r_{cyl}$ and (b) $0.9 \times r_{cyl}$ were unable to achieve a 100% transmission rate, (e) $0.6 \times r_{cyl}$ and (f) $0.5 \times r_{cyl}$ were requiring much higher voltages. (c) $0.8 \times r_{cyl}$ and (d) $0.7 \times r_{cyl}$ offered a good compromise between voltage and transmission.

In figure 4.12 a compilation of screenshots made for optimal settings of each step of the geometry optimization described above is shown. Table 4.2 presents the voltages that were used for fig. 4.12 and were determined to be the best possible results based on the values of the metric function:

$$f_{metric} = N \cdot m + \sqrt{\overline{z}^2 + \overline{y}^2} \tag{4.2}$$

where N is the number of particles hitting electrodes before reaching the target, m is the multiplier with which those losses are weighted, and z and y are the positions of the particles. This function plays a crucial role in the decision-making process of the optimizer, determining whether currently tested settings are superior to the previous ones and whether it is necessary to replace them. The f_{metric} value serves as an indicator of desirability for the optimizer with lower values being perceived as more favorable. Given that spot size is the key quality of the beam for the annihilation studies, this metric primarily focuses on the position of particles on the test plane, aiming to focus them at the center of the foil's intended position. To prevent the optimizer from repeatedly

obtaining the same f_{metric} values by prematurely losing the beam, the number of particles that annihilated on electrodes before reaching the target (N) was factored in with a multiplier (m). Additionally, the average position of multiple particles was considered to find a solution suited for the beam. This approach ensured that even if all particles hit the electrodes, the metric value would not drop to zero, preventing the optimizer from simply lowering the metric by annihilating all or a part of the particles elsewhere instead of reaching the target. The resulting optimized geometry can be seen in fig. 4.13.

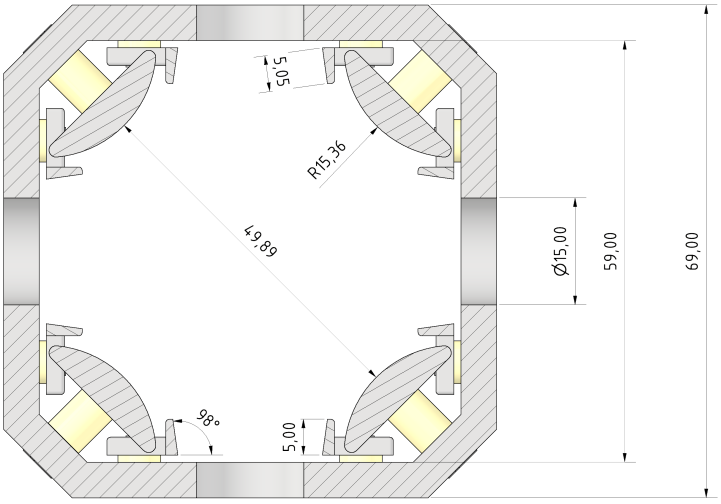

Figure 4.13.: Drawing of the quadrupole bender. The dimensions are based on the results from figure 4.12, taking into account constraints in the applied voltages to 2 keV and feasibility of machining. The yellow structures are made of polyetheretherketone (PEEK) for isolation purposes. Electrodes and the rest of the housing are made of aluminum.

4.3.2. Einzel lenses

An Einzel lens is a type of electrostatic lens used to focus charged particle beams. Electrostatic lenses consist of at least two but usually three or more electrodes, with the electrodes being held at a different potentials [39]. Although cylindrical shapes are the norm, other shapes can be used too [41]. The name Einzel refers to a configuration where the middle ring is set on a different voltage than the other two rings sharing the same potential. These lenses exhibit lower aberration coefficients than lenses with different potentials on all ring electrodes. The potential difference creates an electric field that converges towards the center of the lens, which causes the charged particles to be focused towards a point. Particles that pass through this field gradually get pushed towards the middle of the cylinders. This is different than in optical lenses, where the change in trajectory is more immediate because of the instant change at the boundary. However, similar to optical lenses, only the region at approximately a quarter of the inner diameter of an Einzel lens is relatively free of aberrations [42].

An Einzel lens with a split electrode middle ring is a modification to the traditional Einzel lens design that includes a gap or split in the central electrode. This split creates two separate regions of higher voltage, which causes the electric field to be concentrated in two distinct areas [43]. These two areas can be used to push the particles passing through the electrodes in a given direction if two different potentials are applied on these segments. For steering in multiple different directions a greater number of cuts and potentials can be included in the center electrode. By splitting the middle ring of a cylindrical lens diagonally, these Einzel lenses introduce less aberrations to a beam. This special type of lens is often referred to as Sikler-type Einzel lens [39, 43, 44]. Additionally, the split electrode design allows for greater flexibility in controlling the shape and intensity of the focused beams, which can be important for optimizing the performance of a lens for a particular application.

(a)

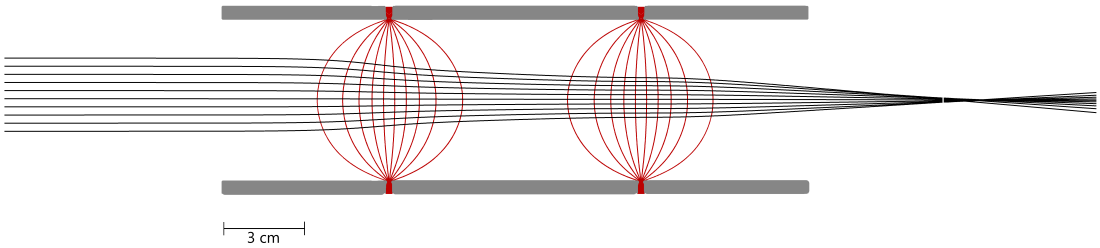

(b)

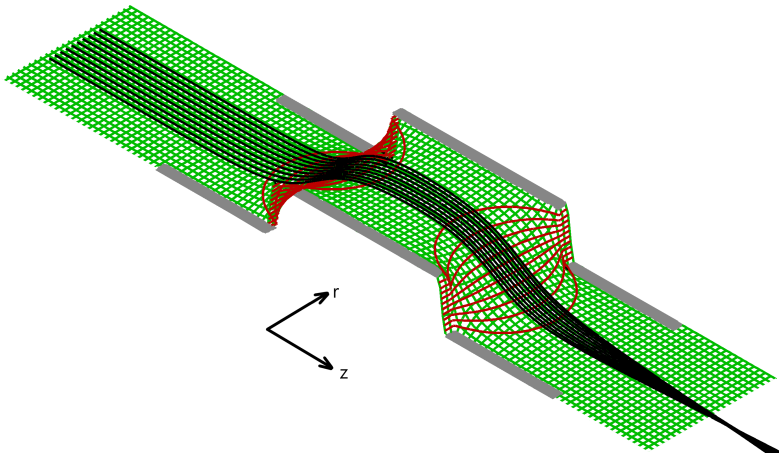

Figure 4.14.: (a) Contour plots for the cross-section of a 60 mm diameter cylindrical Einzel lens with its potential set to 500 V on the middle ring and the other two electrodes set to ground, focusing a beam of 250 eV antiprotons. The resulting trajectories of the particles through the lens are depicted in black, the electrodes in gray and the field lines of the potential in red. (b) PE view for the $\overline{\mathrm{p}}$ in the Einzel lens.

(a)

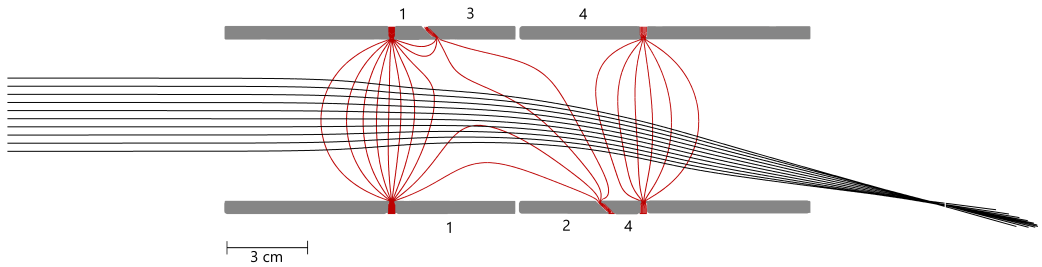

(b)

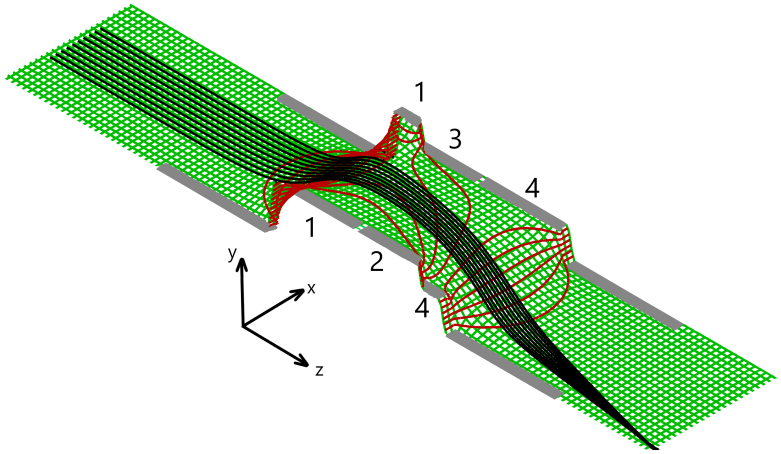

Figure 4.15.: Contour plots of a 60 mm diameter Sikler-type Einzel with two diagonal cuts, creating 4 different segments in the middle ring. Its potentials are set to 300 V for the electrodes marked as 3 and 4, and 500 V for electrodes 1 and 2, the outer two ring electrodes are set to ground, focusing a beam of 250 eV antiprotons. The resulting trajectories of the particles through the lens are depicted in black, the electrodes in gray and the field lines of the potential in red. (b) PE view for said $\overline{\mathrm{p}}$ in the Sikler-type Einzel lens.

The usual proportions for the rings of a cylindrical Einzel lens are at a 1:1 ratio for the diameter D and the length L [45]. Because of the size constraints of the six-way cross this had to be adapted for this application, as can be seen in fig. 4.16. E1 is affected by this problem, as it has to be big enough as to accept the full diameter of the the beam from MUSASHI, whereas its length was predetermined by its position, as described in the previous section.

This was achieved by reducing the length L of each of the rings to half their diameter D, which resulted in a reduction of the total length to fit inside of the MUSASHI-side port of the cross (fig. 4.11).

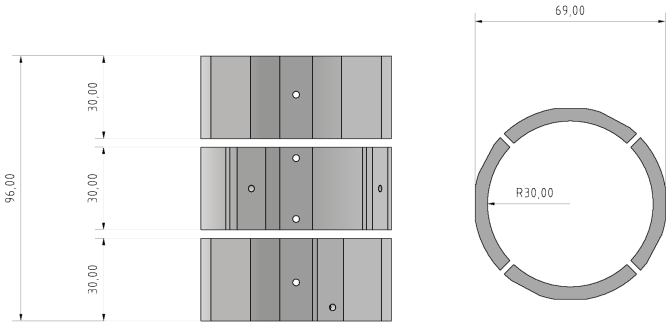

Figure 4.16.: Schematics for E1, where the middle ring is split in four equal parts by cutting it along two 90° planes passing through the center of the cylinder. Each segment can be set on a different potential, thereby changing the shape of the field inside.

In fig. 4.17 the design used for the other Einzel lenses after the deflector is shown. At first different length middle rings and cut shapes were tested, based on the design of E1. By stretching in the z-direction, to make use of all the available space, lenses with the same angle of cuts but different length middle rings were simulated. To keep the results comparable, the same beam and electrode diameter for the ring electrodes of the Einzel lenses was used for different ratios of ring lengths. In fig. 4.19 the different beam shapes produced by the different tested Einzel lenses are shown. The same input beam of 10^5 particles from a homogeneous circular distribution with a 10 mm radius is used, moving in directions that are evenly distributed within 1° from the z-axis, with a uniform energy spread between 249 and 251 eV. This was focused with 500 V on each segment of the middle ring by different Einzel lenses. These runs were then repeated, but for each Einzel lens the beam was deflected downwards by lowering one segments potential by 200 V. All the Einzel lens designs were compared with an inner diameter of 60 mm and the length adjusted according to that. The beam-profiles shown were taken at 400 mm from the entrance of the first ring. The results from fig. 4.19 (a) show the behavior of the design used for E1, as shown in fig. 4.16, while fig. 4.19 (b) and fig. 4.19 (c) show what effect stretching the middle electrode would have on the beam shape for the same cuts. Although deflection of the beam is increased with the same potentials, the quality of the beam suffers with the designs derived from E1. To keep the quality of the $\overline{\text{p}}$-beam at the target distance as high as possible, the design of the Sikler-type Einzel lens, as shown in fig. 4.17, was adapted for the remaining two Einzel lenses.

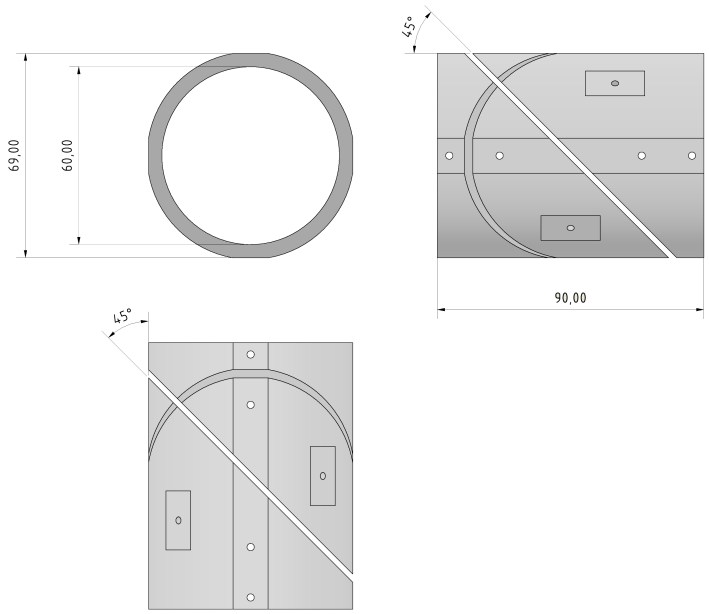

Figure 4.17.: Schematics of the middle ring of a Sikler-type steering Einzel lens. Design used for E3. E2 uses the same proportions, but smaller dimensions.

4.4. Voltage Optimization

After fixing the geometry for our setup at $0.75 \times r_{cyl}$, the voltages were optimized by a Lua code that repeatedly ran a simplex optimizer. Each completed cycle was ended by saving the optimized values for f_{metric}, the potentials for each electrode and the number of particles that did not reach the test plane into a file for future reference. For each rerun, the newly determined minima were used to replace the starting values of the previous run. However, they were changed by a randomly generated step before the optimization process was restarted for the same electrodes. By repeatedly performing simulations with slightly different starting values, the probability to find multiple different minima increases. Multiple repetitions of this process were performed for every set of electrodes on four different potentials.
The order the electrode sets were optimized in was:

- E1
- E2
- quadrupole deflector

A short summary of the evolution of f_{metric} can be seen in table 4.3. Each row represents the optimization of one set of electrodes. By comparing the lines, the impact of each

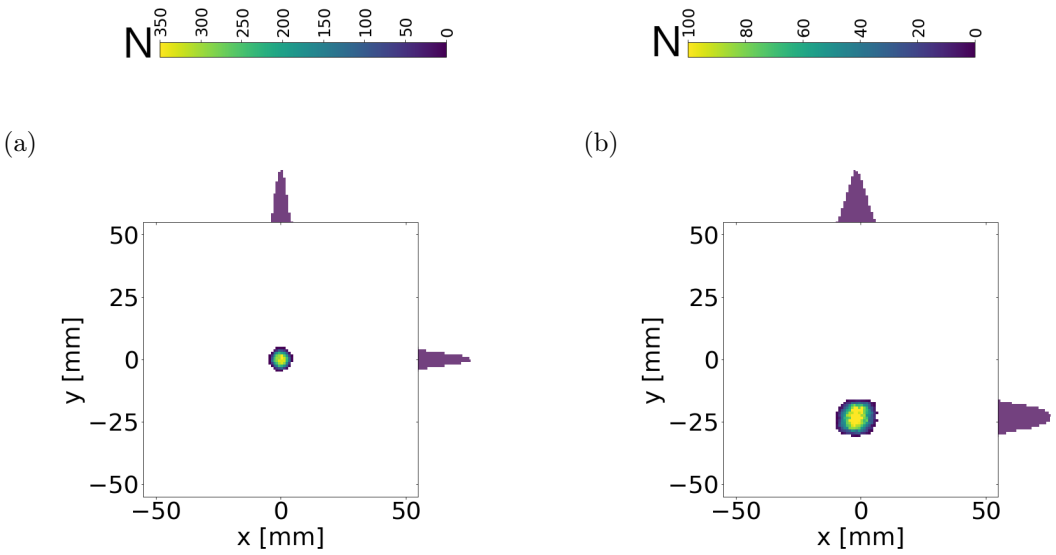

Figure 4.18.: Beam-profiles of 10 mm flat circle distribution measured at 400 mm after entering a Sikler-type Einzel lens with a 3:2 length to diameter ratio for the middle ring and two 45° cuts. (a) 500 V potential was set on all segments of the middle ring. (b) three segments are at 500 V and one segment's potential is at 300 V.

optimization on the quality of the beam can be observed, the biggest jump being after adjusting E1 as fewer particles got annihilated.

Table 4.3.: Optimization of the applied voltages for E1, E2 and the quadrupole deflector. Every step in the table shows the best voltages after multiple randomized runs of the simplex optimizer. On the left side the sinking value of f_{metric} for each of this steps is shown. All values are shown in [V] (electrode names according to appendix A).

	E1				**E2**				**Quadrupole deflector**			
f_{metric}	P_{E1-1}	P_{E1-2}	P_{E1-3}	P_{E1-4}	P_{E2-1}	P_{E2-2}	P_{E2-3}	P_{E2-4}	P_{R_1}	P_{R_2}	P_{S_1}	P_{S_2}
7766.35	800.00	800.00	800.00	800.00	200.00	200.00	200.00	200.00	-800.00	800.00	-300.00	300.00
55.21	1481.28	1449.71	1597.67	1531.88	200.00	200.00	200.00	200.00	-800.00	800.00	-300.00	300.00
24.61	1481.28	1449.71	1597.67	1531.88	257.74	208.97	240.10	265.34	-800.00	800.00	-300.00	300.00
22.26	1481.28	1449.71	1597.67	1531.88	257.74	208.97	240.10	265.34	-1476.24	1404.81	173.10	-18.87

4.5. Resolution

Mesh sizes chosen for simulations are important for each step of the trajectory calculation as mentioned in section 3.5.1. If the GU is not chosen to be small enough, the resolution of the PA can negatively affect the accuracy of the simulation. One way to assess this is to repeatedly rerun a simulation with the same voltage and geometry, while changing

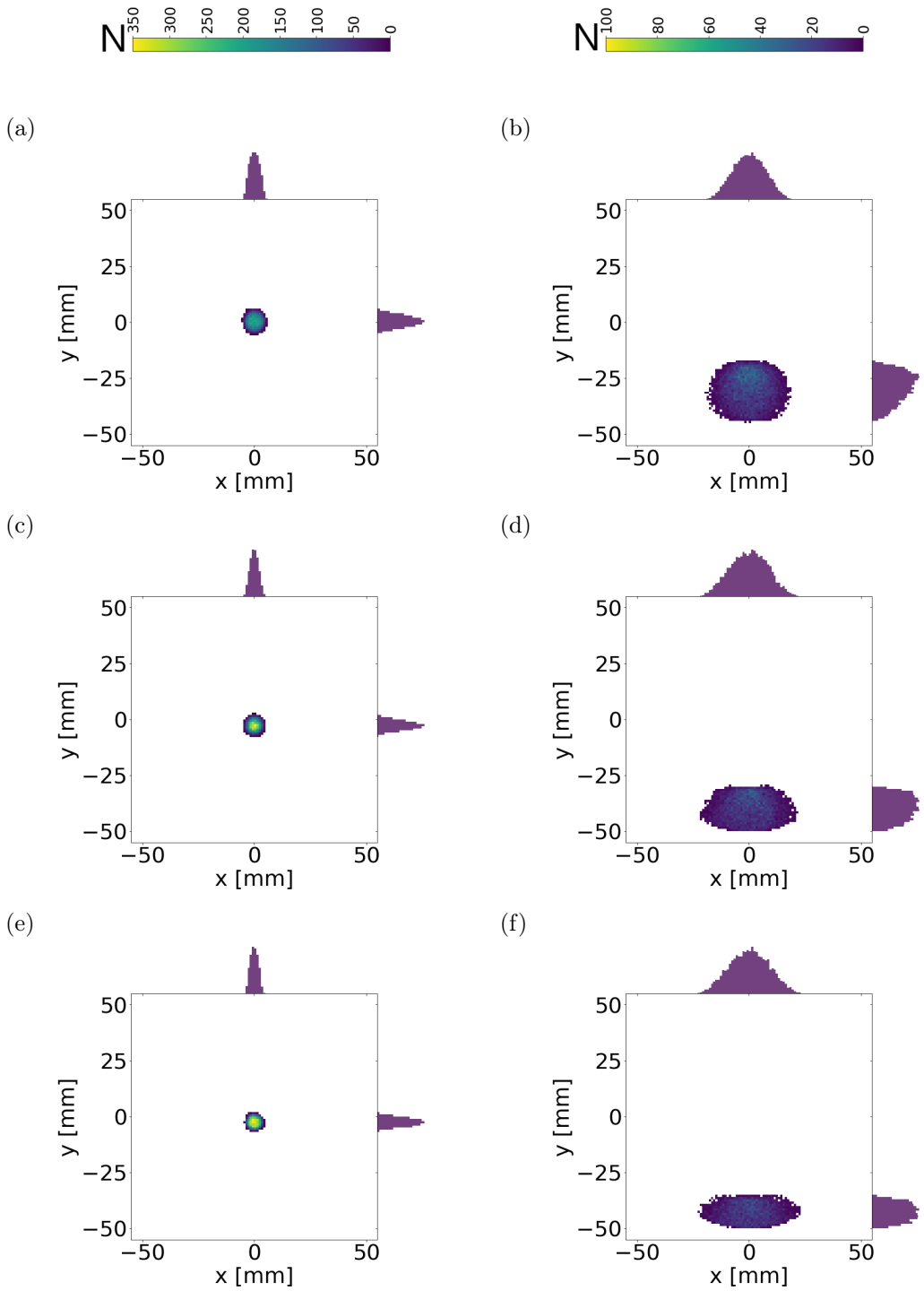

Figure 4.19.: Beam-profiles of 10 mm diameter homogeneous circular distribution measured at 400 mm after focusing through a Steering Einzel lens with split electrodes with (a,b) a 1:2 length to diameter ratio, (c,d) a 1:1 length to diameter ratio and (d,e) a 3:2 length to diameter ratio. Left side: a 500 V potential is set on all segments of the middle ring. Right side: one segment's potential is lowered to 300 V.

the resolution. This was done with a PA of the quadrupole deflector, E1, E2 and the six-way cross. As the results change with the mesh size, the optimal potentials also start to differ slightly. However, for these tests this is irrelevant, as the voltages used do not have to be the optimal ones, it is only important to keep the potentials for each of these runs the same. Hence a single array file (no independently adjustable electrodes), with fixed potentials was used to reduce the time spent refining the array for each run of the simulation. By reusing the solutions of each run to start the refining process of the next run, solutions can be reused without having to restart the calculations for the field (a more detailed explanation for this can be found in [29, 30]). The effect of increasing the simulation resolution on the beam is illustrated in fig. 4.20. The 100 particles were directed towards the bending set-up from fig. 4.7 equally distributed on the circumference of a 2.5 mm circle with 250 eV. The position of all the particles were saved for each of these runs at the same test-plane at z = 1.7 m and y =0.29 m. The results vary but begin to converge with smaller sizes for the cubic graphical unit (GU) [30].

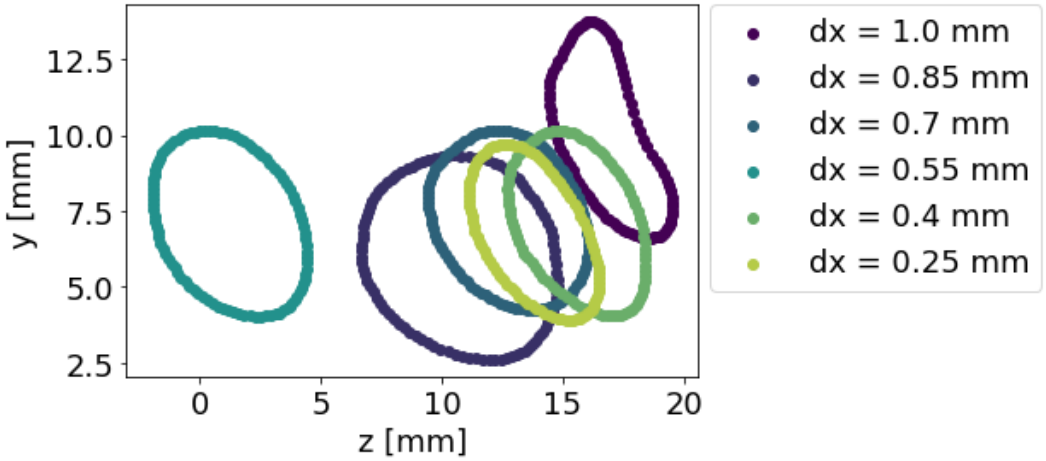

Figure 4.20.: Scatterplot showing the gradual change in the position of a beam consisting of 100 particles arranged in a 2.5 mm radius circle with 250 eV, after being bent by the deflector, while changing the resolution of the PA. Each run reduces the GU size used in the PA.

For memory saving purposes one could also test anisotropically scaled GU. This is useful for instances where the charged particles are not expected to move in a certain dimension over longer distances. In this particular simulation this is never the case, as the bending requires high resolution in two dimensions, while the deflection of the particles by the Lorentz-force of the magnetic coils and the correction through the Einzel lenses requires the resolution to be high in the third dimension.

5. Simulations and Results

Following the characterization described in the previous chapter and after the designs for each part were fixed, the combined performance of all the elements was evaluated. At first, a sub-system consisting of E1, the deflector and E2 was tested. After this, E3 was added. The properties of the beams resulting from the following three configurations

- E1, deflector, and E2
- E1, deflector, E2, and E3 at the GV3 (see fig. 5.1)
- E1, deflector, E2, and E3 close to target position (see fig. 5.3)

were analyzed, the results of which can be seen in table 5.1.
Figure 5.1 shows one of these configurations, where E3 is mounted directly after GV3 between the deflector and the target. The housing of the deflector is used to mount E2 with PEEK mounts and is then connected to an actuator, making a large portion of the bending setup retractable for the purposes described in chapter 4.

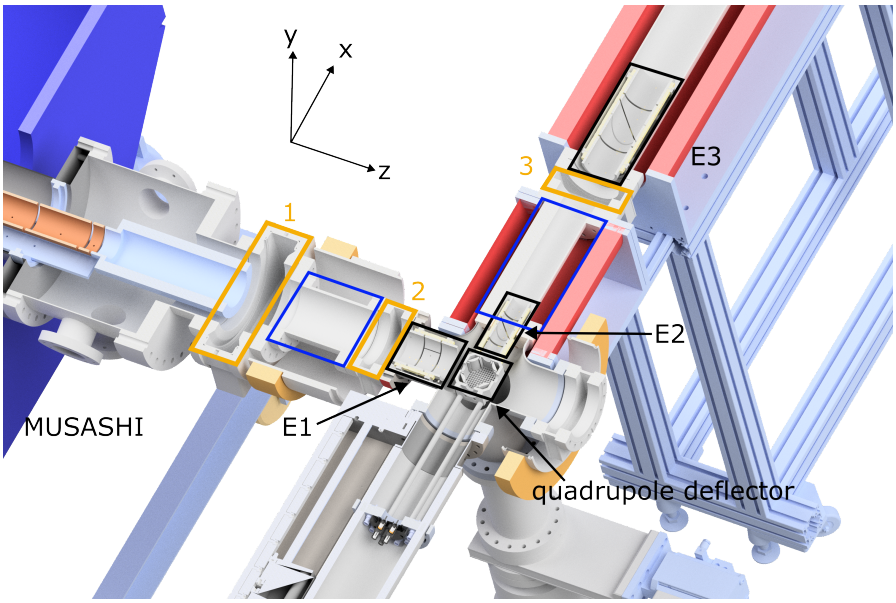

Figure 5.1.: Schematic diagram of the different parts that were tested in the previous chapter. Bellows marked in blue, GV in orange.

In table 5.1, a summary of the change in transmission between the three setups is shown. Each configuration was tested using 10^5 $\overline{\text{p}}$ from MUSASHI (as explained in section 4.1)

in a small 0.5 mm radius distribution, and then another 10^5 particles were injected in a circular distribution with a 5 mm radius to mimic the halo.

Table 5.1.: Results for the particle transmission for each of the possible setups with potentials optimized for spot size.

configuration	transmission in %	transmitted $\overline{p}$	input $\overline{p}$
E1 and E2 only	59	9920	16729
E3 at GV	70	11002	15647
E3 close to target	54	8656	15999

The transmission increases in table 5.1 when E3 is included at GV3, however, if it is placed closer to the target transmission drops in comparison to the reduced set-up. This drop is caused by E3 blocking some of the particles, thereby causing annihilation on its electrodes. This is however an acceptable trade-off for the reduction in beam spot size it provides. The foil size will be 1 cm^2 increasing the importance of the beam spot size in comparison to a slight gain in transmission.

To make the results for the different configurations comparable, the plots in the following three sections and section 5.2 all have a resolution of 1 mm in x- and y-direction for the beam-profiles. The profiles for the input beams are measured at the position of GV2 1.5 m from the center of MUSASHI on the z-axis, while the beam-profiles of the output beam are measured at x = 2.16 m and z = 1.7 m (see fig. 2.9). For ease of reading the axes for the output beam profiles are centered on the target. The histograms for the velocities perpendicular to the direction of the beam have a resolution of 0.4 mm/µs. The energy distributions have a resolution of 0.03 eV.

5.1. Set-up with two Einzel lenses

Fig. 5.2 depicts the input and output beam of a configuration consisting only of the deflector, E1 and E2. Because of space limitations for their mounting inside the apparatus, these three parts stay at the same location for all the simulations performed in this chapter. A configuration consisting only of these parts would mainly have the advantage that its installation would not require opening the positron beam-line. With only two Einzel lenses used, the resulting beam is not well centered and covers a wide area at the target position. The beam size is too large for this use-case. The low spread in velocities perpendicular to the propagation direction of the beam indicates that this result can be improved upon with further focusing elements.

5.2. Set-up with three Einzel lenses

To further improve the focusing of the beam on the target foil a third Einzel lens was used. Its placement in the e^+ beam-line allows a larger diameter than the one for E2 (for

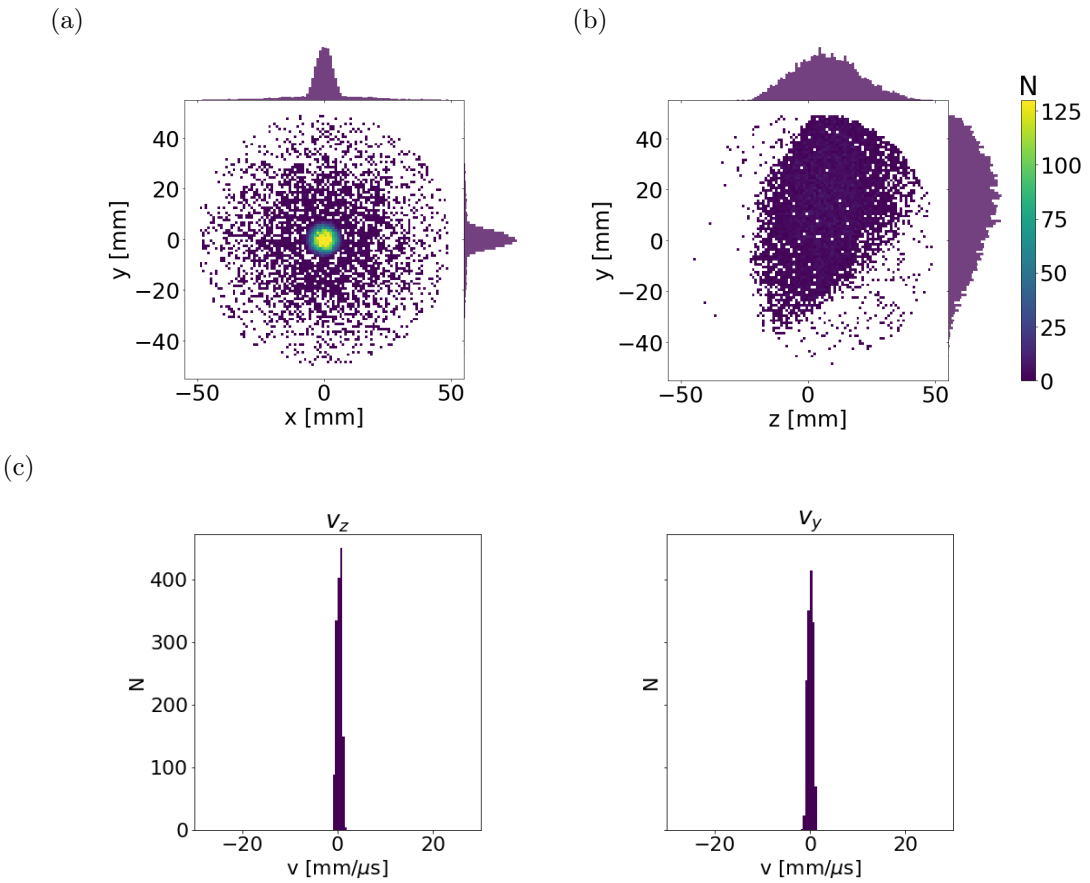

Figure 5.2.: Beam-profiles of the (a) input and (b) output beam for the configuration with only two Einzel lenses. (c) Histograms showing the particles velocity components orthogonal to the x-direction in the target plane.

an explanation see. section 4.3.2). It was expected, that E3 closer to the bender would have beneficial effects on the number of particles arriving at the target position, as the beam entering the Einzel lens would not have had time or space to diverge. However focusing to a small spot size was expected to be superior with an Einzel lens positioned closer to the target.

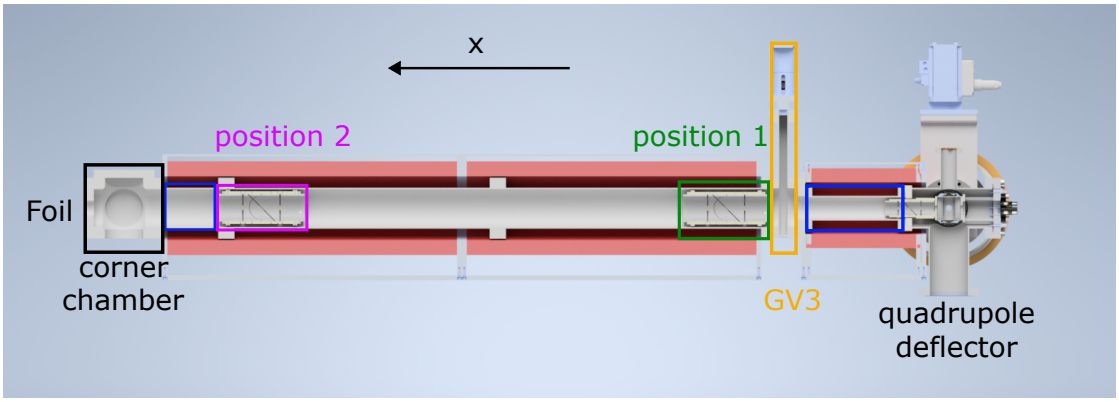

Figure 5.3.: Schematic diagram showing the two possible positions of the third Einzel lens. The orange rectangle marks the position closer to the detector on the left side. The green rectangle marks the position after GV3. Bellows are marked in blue.

In fig. 5.3 the limiting factors for the positions of E3 can be seen. On the left its position is limited by the bellow connecting the corner chamber, so that it can not be moved closer towards the target foil. On the right another bellow and GV3 are reducing the available space. The characteristics of the resulting beam for the position of E3 marked in green, henceforth referred to as 'position 1' in fig. 5.3 are plotted in fig. 5.4. Although the total transmission is improved upon in respect to the configuration with only two Einzel lenses, the now elliptical center part of the beam still increased in size. It would cover an area of nearly 2 cm^2, thus being sub-optimal for the use in annihilation studies, with the target foil covering 1 cm^2 , as mentioned before.

In table 5.1 it is shown how the transmission of the two possible configurations with three Einzel lenses differs. Moving the lens closer to the target makes the velocity spread of the beam diverge, but it also reduces its spot size significantly. Since this configuration produced promising results (fig. 5.5), further runs were performed to ensure that transport would be possible, even if the spatial expansion of the $\overline{p}$ cloud would be bigger than expected. Therefore a beam generated from a 1 mm diameter circular distribution in MUSASHI was investigated with the same settings and the same set-up. The results of this run can be seen in fig. 5.6.

In table 5.2 and table 5.3 a summary of the beam characteristics resulting from the configurations described in the previous three sections is given. Comparing the results

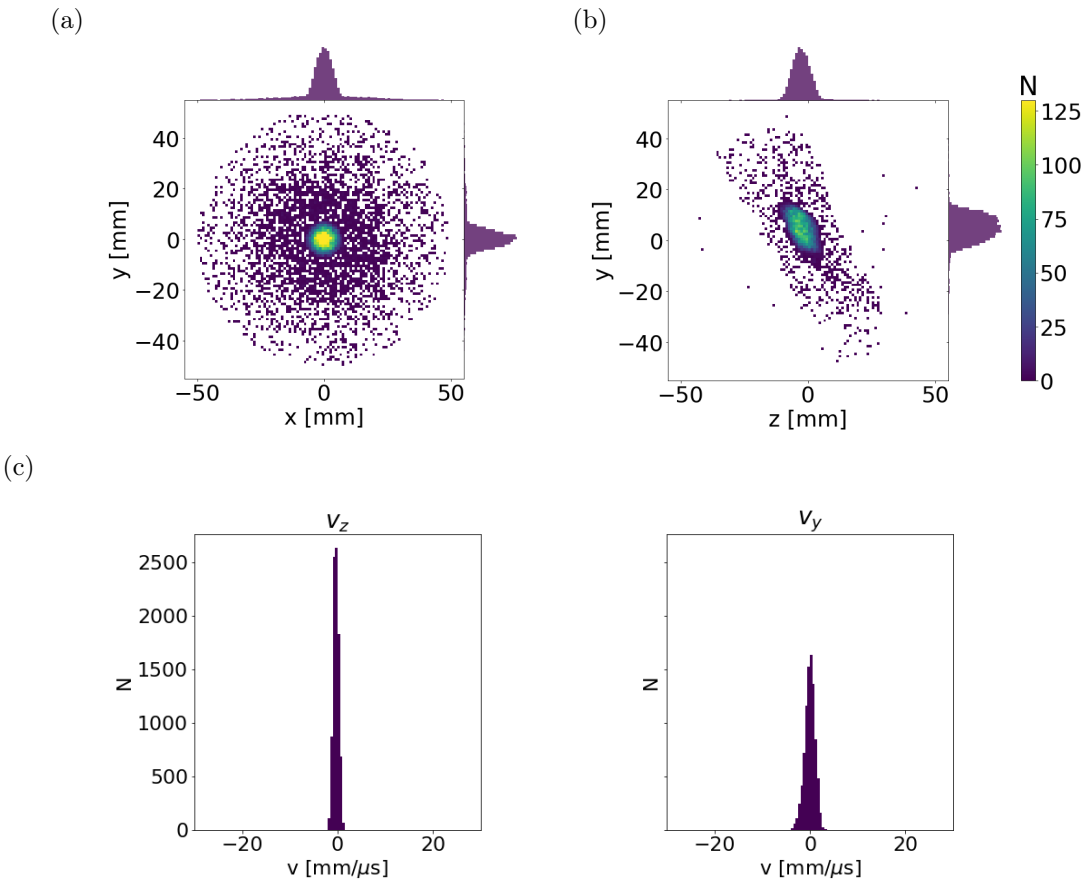

Figure 5.4.: Beam-profiles of the (a) input and (b) output beam for the set-up with with the third Einzel after GV3 (position 1). (c) Histograms showing the particles velocity components orthogonal to the x-direction in the target plane.

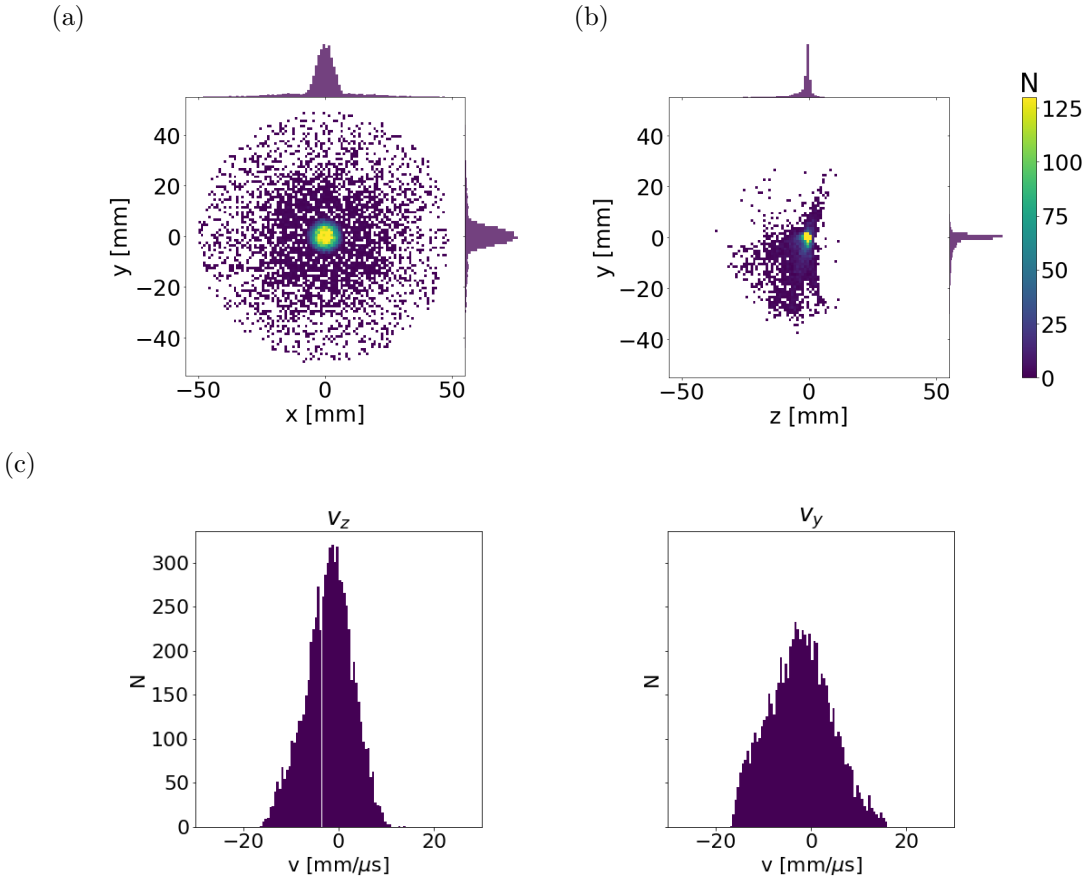

Figure 5.5.: Beam-profiles of the (a) input and (b) output beam for the set-up with with the third Einzel as close as possible to the target foil (position 2). (c) Histograms showing the particles velocity components orthogonal to the x-direction in the target plane.

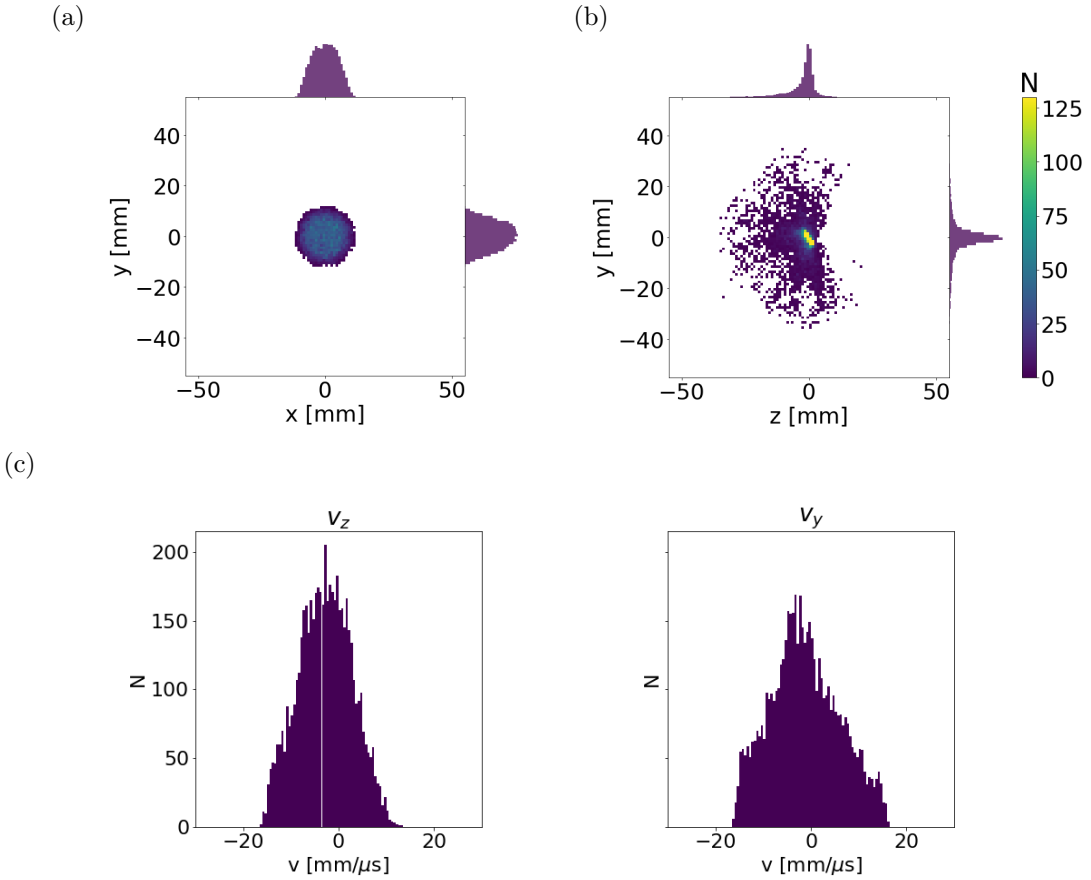

Figure 5.6.: Beam-profiles of a (a) input beam with a 1 mm homogeneous circular distribution and (b) its output beam after the bending, with E3 at position 2. (c) Histograms showing the particles velocity components orthogonal to the x-direction in the target plane.

Table 5.2.: Summary of the transmission and the spread of the velocities for a beam with a typical distribution of halo and compressed center (see section 4.1). All three configurations discussed in this chapter are compared.

Name	Transmission [%]			average value	std dev σ
E1 and E2 only	59	z	[mm]	7.41	12.92
		y	[mm]	12.43	19.04
		v_z	[mm/µs]	0.95	1.24
		v_y	[mm/µs]	1.27	1.84
		E_{kin}	[eV]	250.29	0.57
E3 position 1	70	z	[mm]	−2.54	4.91
		y	[mm]	4.69	7.23
		v_z	[mm/µs]	−0.46	0.91
		v_y	[mm/µs]	0.15	1.41
		E_{kin}	[eV]	250.33	0.57
E3 position 2	54	z	[mm]	−2.11	4.22
		y	[mm]	−2.64	6.69
		v_z	[mm/µs]	−2.94	5.93
		v_y	[mm/µs]	−4.27	8.73
		E_{kin}	[eV]	250.28	0.57

from the tables, it is clear that three Einzel lenses are necessary whether the goal is to maximize the transmission or to minimize the beam spot size. While the data from table 5.2 and table 5.3 suggest that the difference between the two set-ups including E3 is negligible, the beam-profiles (fig. 5.5 and fig. 5.4) highlight the differences in beam shape. As the focus in our case lies on the reliable transmission of $\overline{\text{p}}$ onto a small target, the superior distribution achieved by placing E3 as close to the target foil as possible (see fig. 5.5), is of greater value than the higher transmissions and low divergence provided by having E3 close to the quadrupole deflector (see fig. 5.4).

5.3. Halo

The simulations conducted with the configurations described in section 5.1 and section 5.2 demonstrate the feasibility of bending a significant portion of the beam with satisfactory quality onto the target foil. The transmission losses presented in table 5.1 mainly occur due to particles forming the beam's halo, which subsequently annihilate either on the surface of E3 or the beam-line wall, with most of the annihilations occurring before the six-way cross. This effect is particularly noticeable when E3 is positioned in close proximity to the target. Comparing table 5.2 with table 5.3, particularly focusing on the transmission, reveals that the majority of particles which annihilate originate from the 5 mm distribution. As depicted in fig. 5.7, the beam's halo not only occupies a large surface area, but its particles also exhibit a wider range of velocities in the x- and

Table 5.3.: Summary of the transmission and the spread of the velocity of the beams of all three configurations discussed in this chapter. Only the center 0.5 mm diameter part of the beam was used for this table.

Name	Transmission [%]			average value	std dev σ
E1 and E2 only	88	z	[mm]	7.18	12.46
		y	[mm]	12.98	18.45
		v_z	[mm/µs]	0.92	1.19
		v_y	[mm/µs]	1.33	1.75
		E_{kin}	[eV]	250.29	0.57
E3 position 1	100	z	[mm]	−2.76	3.12
		y	[mm]	4.92	4.48
		v_z	[mm/µs]	−0.49	0.64
		v_y	[mm/µs]	0.14	1.09
		E_{kin}	[eV]	250.33	0.57
E3 position 2	82	z	[mm]	−2.07	4.07
		y	[mm]	−2.73	6.64
		v_z	[mm/µs]	−2.89	5.81
		v_y	[mm/µs]	−4.45	8.61
		E_{kin}	[eV]	250.29	0.57

y-directions (see fig. 4.5 for a comparison). As particles exit MUSASHI further away from the axis, they are increasingly affected by the expanding solenoid field. Consequently, the closer these particles approach the pipe's edge, the more challenging it becomes to recover them. In a pipe with a 100 mm diameter, the Einzel lens and quadrupole cannot be sufficiently large to significantly enhance the transmission of particles deviating too far from the beam axis.

Because of the large area the trajectories of the 10^5 halo-particles are distributed over, only about 45% make it to the six-way cross. Within this relatively broad distribution, only those particles closest to the center manage to navigate through the bending process. This observation becomes particularly evident when examining fig. 5.8, where the beam profile on the target plane in fig. 5.8(a) closely resembles the profile depicted in fig. 5.5.

Figure 5.9 depicts an additional visualization by overlaying the beam shapes of different starting distributions, while maintaining an equal number of particles at the target position. Despite the variations in the initial distributions, the resulting beam shapes are similar. This observation suggests that the majority of particles successfully navigating the bending process and reaching the target originate from the central region of the wider distributions.

As demonstrated in section 5.2, the configuration incorporating a third Einzel lens near the target foil can yield a favorable spot size, which could potentially be further enhanced by implementing an aperture to restrict the halo. However, this approach presents two potential challenges directly related to the aperture's placement. If positioned within the

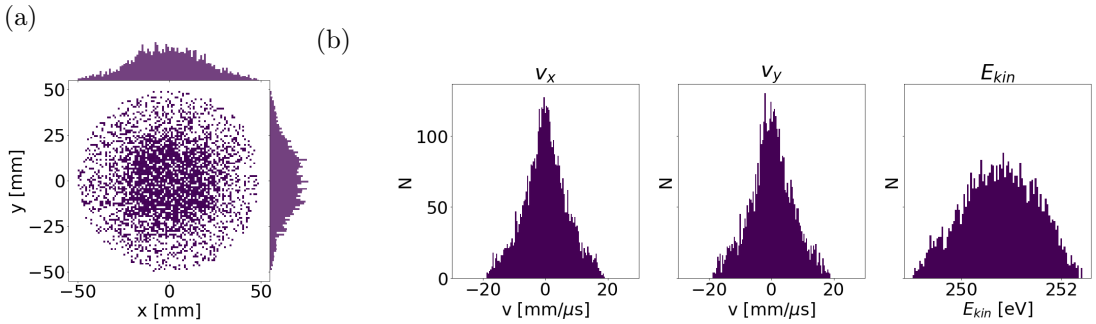

Figure 5.7.: Distribution of the 5 mm $\overline{\text{p}}$ halo at the gate valve before the double cross. The particles emerging from the halo part of the plasma account for most of the spread in velocities perpendicular to the propagation direction of the beam.

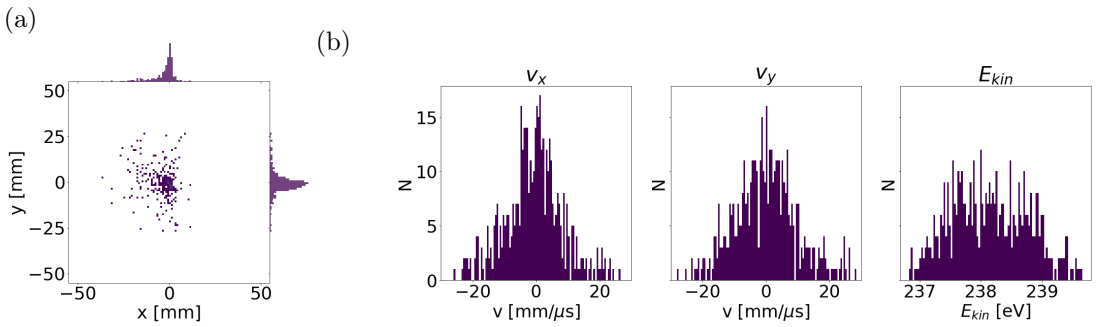

Figure 5.8.: Distribution of the 5 mm $\overline{\text{p}}$ halo at the position of the target foil. Only about 10% of the particles from the halo can make it through the bending. As these particles have a relatively flat distribution when arriving at the gate valve, only the particles in the center of that distribution make it through the bending.

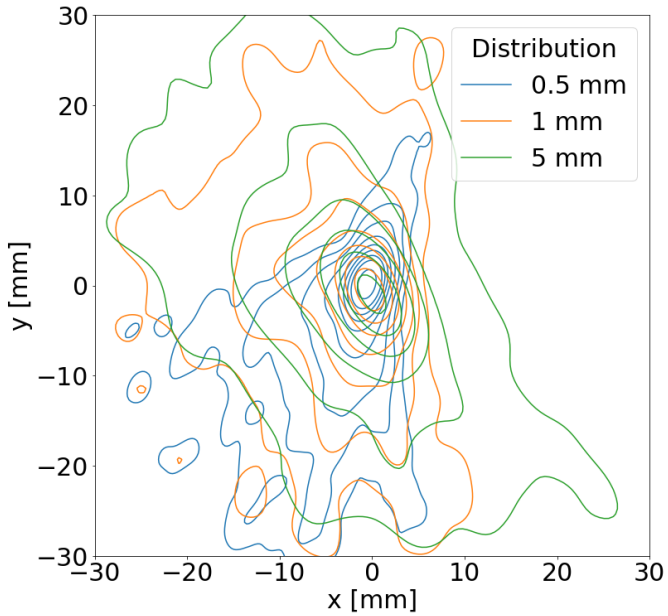

Figure 5.9.: Kernel density estimate (KDE) plot of 4655 particles for a starting diameter of 0.5, 1 and 5 mm.

positron beam-line, it may lead to a decrease in the available positrons for the mixing experiment. Conversely, locating the aperture closer to the target position could result in annihilation events occurring in close proximity to the detector, thereby compromising the accuracy of the reconstructed target foil annihilations.

5.4. Kinetic Energy and Accuracy

To ensure, that particle transport between PA instances is physical, sanity checks of the particle energy can be performed. As mentioned in section 4.1 the $\overline{\mathrm{p}}$ start on a -250 V potential and with a spread of 0 to 2 eV. Because of the conservation of kinetic energy and the target being set to 0 V we expect approximately 250 eV for the particles energy at the target.

The simulation used to generate the data for this chapter consisted of three separate PAs:

- MUSASHI trap (cylinder symmetrical)
- the six-way cross consisting of E1, the quadrupole deflector and E2 (planar)
- E3 (planar)

In the case of the last PA, appropriate adjustments were made to ensure that the sizes were properly matched, allowing the Neumann conditions on the edges to correspond to

zero. However, as depicted in fig. 4.7, the boundary of the second array on the MUSASHI side are positioned too closely to the electrodes, making it impossible for the potential to reach 0 V. To address this issue, SIMION employs a linear approximation method to estimate the energy of particles between two separate arrays in a simulation, even when they are not within GUs of one and, as a result, not subject to complete trajectory calculations. The simulations confirmed that most of the particles that reach the target have an energy of 250 eV, as shown in table 5.2 and table 5.3, where the energy stays close to the expected value and its standard deviation is low. Interestingly, the isolated halo does have a much broader distribution in energies as can be seen in fig. 5.7 and fig. 5.8.

5.5. Construction and Materials

For the construction of the parts in the transport line, multiple factors such as:

- the operation in ultra high vacuum (UHV)
  - low hydrocarbons for e^+ annihilation
- magnetic properties due to e^+ transport
- secondary electron emission (SEE) and secondary electron yield (SEY)
- compatibility with high voltages
- weight
- cost efficiency
- feasibility of machining

had to be taken into consideration. Aluminum was chosen due to its cost efficiency and ease of machining, making it more suitable for the application described in this thesis compared to non-magnetizable steel or copper. To secure each electrode in place, screws made of non-magnetizable steel were used, fastened to a glas-fiber reinforced polyetheretherketone (PEEK) rails. The choice of PEEK was based on its insulating properties and compatibility with UHV (ultra-high vacuum) environments, which are crucial factors in this application. In fig. 5.10 a photograph of the electrodes can be seen while in fig. 5.11 a photograph of the manipulator is shown.

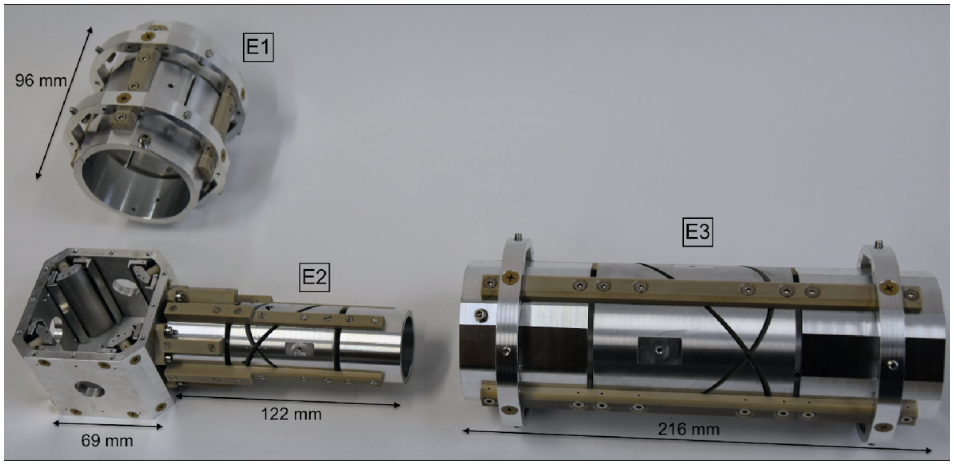

Figure 5.10.: Photograph of the machined parts. Aluminum was chosen as the material for the electrodes. The electrodes are held together by rails made out of glass-fiber reinforced PEEK [23].

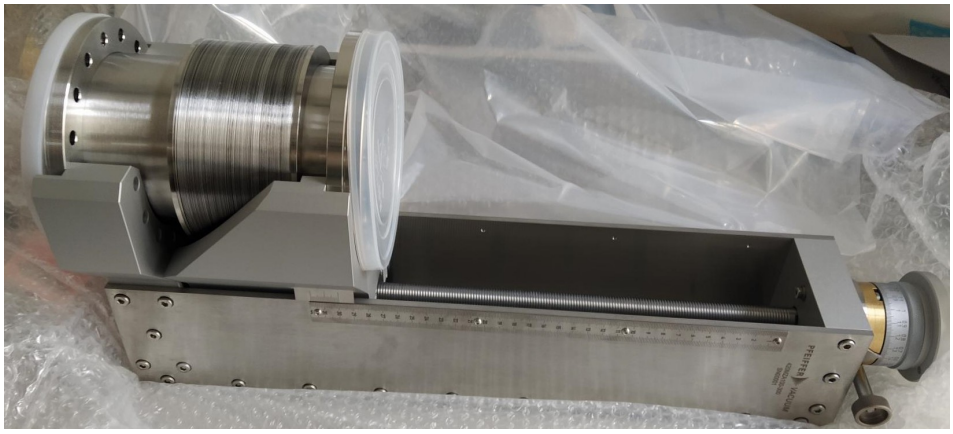

Figure 5.11.: Photograph of the manipulator to be used with the deflector and E2.

One disadvantage of using aluminum is its high Secondary Electron Emission (SEE) when its surface oxidizes. Since a significant portion of the antiprotons is lost due to annihilation with the electrodes, minimizing SEE is crucial to limit the emission of electrons into the transport line, which could negatively impact the antihydrogen experiment. To address this issue, the electrodes are coated with colloidal graphite on the surfaces facing the particles that come into close proximity with the traveling $\overline{\mathrm{p}}$. The effects of graphite coatings on aluminum can be observed in fig. 5.12. As shown there, aluminum treated with a carbon coating exhibits consistently lower SEE values throughout the measured range compared to untreated aluminum. A photograph of the carbon-coated parts is included in fig. 5.13. In the center of the photograph the perforated lids of the quadrupole housing are visible. These openings serve the purpose of facilitating electrical connections with the shims and rod electrodes (on the right side of the picture) and increasing pumping conductance. Additionally, the uniform graphite coating may help mitigate naturally occurring patch potentials in metals [46]. However, the impact of these potentials on the lenses or deflector is not expected to be significant, as the particles pass through them quickly.

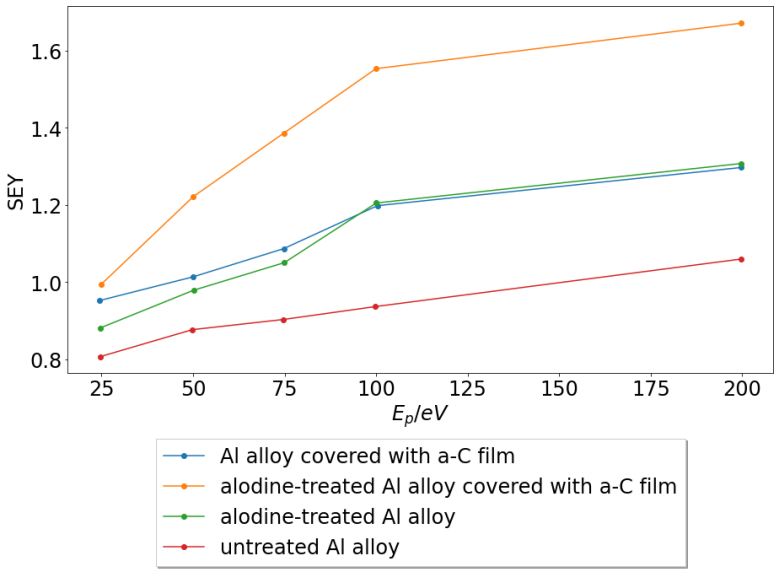

Figure 5.12.: Plot of the secondary electron yield for differently treated Al alloy samples. Data taken from [47].

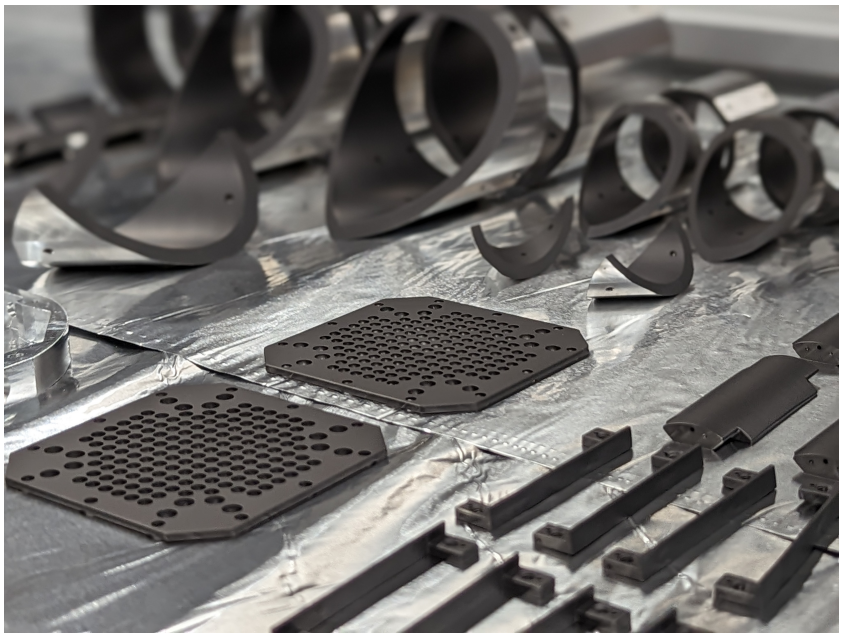

Figure 5.13.: A photograph of the colloidal graphite coating applied to the sides of the electrodes that will be facing the particles.

6. Conclusions and Outlook

The goal of the work done in this thesis is to design a beam-line with the the purpose of transporting slow extracted $\overline{\text{p}}$ from the MUSASHI Penning-Malmberg trap to 1 cm^2 large target foils. For this reason a 90° bend and focusing elements had to be introduced to the beam. The transport was achieved by using simplex optimization for the geometry and the applied voltages on the electrodes of a quadrupole deflector and three different Einzel lenses necessary for the deflection and focusing of the beam.

As discussed in chapter 4, during the previous beam campaign for annihilation studies only around 1000 to 2000 annihilations were detected per AD-cycle. In order to improve on this number and to obtain a configuration where annihilation studies can be performed without vacuum interventions thus allowing fast switching, extensive simulations were conducted to develop a new beam-line specifically tailored for annihilation studies by adapting a part of the existing positron beam-line. The current configuration MUSASHI is able to trap between 2×10^5 and 1.6×10^6 from each $\overline{\text{p}}$-pulse provided by ELENA.

Initially, the focus was on evaluating the beam's properties after the slow extraction. Based on the insights gained from these simulations, the ion optics required for transporting antiprotons to the target foil were designed. So as to not obstruct the production of antihydrogen in the Cusp-trap, a 90° bend had to be introduced between the MUSASHI trap and the Cusp-trap. Since no existing designs provided the matching beam characteristics for our purpose at the target position, various methods were explored to achieve a beam of sufficient quality.

The designed transport system consists of three Einzel lenses and a quadrupole deflector. The design of the quadrupole deflector focused on redirecting particles and minimising annihilations. To achieve this, the proportions of the quadrupole were adjusted using a geometry sweep while optimizing its potentials and geometry. The first lens, E1, serves as a steering lens placed before the bender. Its purpose is to reduce the beam diameter while centering it on the entrance apertures of the deflector in order to increase the number of particles entering the quadrupole. Since the beam passes through the magnetic field generated by two solenoid coils used for beam focusing in the Cusp-trap, E2, a Sikler-type lens, is employed to compensate for the deflection caused by Lorentz forces during the bending process. To minimize radial expansion of the beam on the target foil E3, another Sikler-type Einzel lens is positioned in close proximity to the target. This configuration ensures the beam's radial expansion is kept to a minimum while also providing additional steering capabilities. In the final step of the simulation and design process, the optimization focused on the position of the Einzel lenses and optimizing each

set of four electrodes to achieve the best possible quality.

According to the results in this thesis a 42% transmission to the 1 cm^2 target foil will be achieved, for a beam with a typical distribution of halo and center particles. For an estimated average pulse of 8×10^5 antiprotons, about 3.36×10^4 particles will reach the foil and annihilate on it. The shape of the beam can be seen in fig. 6.1, where a cropped dataset from fig. 5.5 is provided with an increased resolution of Δy, Δz of 0.1 mm. The y-, and z-projections of the beam profile indicate a sufficiently small spot size for annihilation studies. If only the center part of the plasma is taken into account and one assumes that it makes up half of the total particles trapped, then 2.48×10^4 $\overline{p}$ of that part are expected to reach the target foil. In both cases a significantly higher transmission than in previous campaigns is ensured.

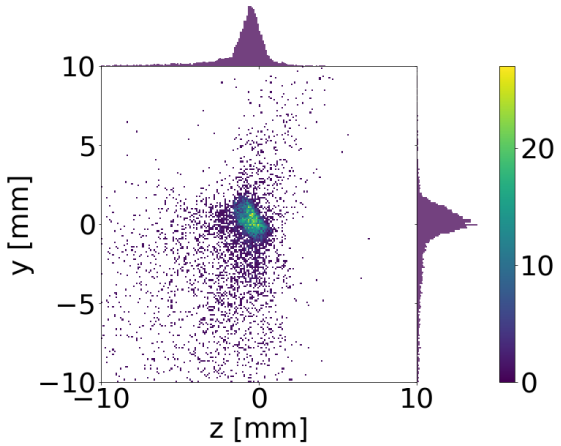

Figure 6.1.: Beam-profile of a 1 cm^2 part at the center of the target distance

At this time, all parts for the $\overline{p}$ transport line described are machined from aluminum, coated with colloidal graphite and assembled at the SMI. High voltage tests, to ensure performance during the operation in the beam campaign, are still pending and will be conducted in Vienna during June 2023. The installation at the ASACUSA experiment is scheduled for early summer this year. The first runs using a position sensitive multi channel plate (MCP) detector at the position of the target foils, to prepare the set-up for the annihilation studies, is planned.

Bibliography

[1] Andrei D Sakharov. "Violation of CP invariance, C asymmetry, and baryon asymmetry of the universe". In: *Soviet Physics Uspekhi* 34.5 (1991), p. 392. ISSN: 0038-5670. DOI: 10.1070/PU1991v034n05ABEH002497. URL: https://dx.doi.org/10.1070/PU1991v034n05ABEH002497.

[2] E Widmann and for the ASACUSA Cusp Collaboration. "Hyperfine Spectroscopy of Antihydrogen, Hydrogen, and Deuterium". In: *Physics of Particles and Nuclei* 53.4 (2022), pp. 790–794. ISSN: 1531-8559. DOI: 10.1134/S1063779622040141. URL: https://doi.org/10.1134/S1063779622040141.

[3] G. Gabrielse et al. "Trapped antihydrogen in its ground state". In: *Physical Review Letters* 108.11 (Mar. 2012). ISSN: 00319007. DOI: 10.1103/PhysRevLett.108.113002.

[4] C. Amole et al. "The ALPHA antihydrogen trapping apparatus". In: *Nuclear Instruments and Methods in Physics Research Section A: Accelerators, Spectrometers, Detectors and Associated Equipment* 735 (Jan. 2014), pp. 319–340. ISSN: 0168-9002. DOI: 10.1016/J.NIMA.2013.09.043.

[5] P. Pérez et al. "The GBAR antimatter gravity experiment". In: *Hyperfine Interactions* 233.1-3 (Aug. 2015), pp. 21–27. ISSN: 15729540. DOI: 10.1007/s10751-015-1154-8.

[6] A. Kellerbauer et al. "The AEGIS experiment at CERN: Measuring the free fall of antihydrogen". In: *Hyperfine Interactions* 209.1-3 (May 2012), pp. 43–49. ISSN: 03043843. DOI: 10.1007/s10751-012-0583-x.

[7] P V Degtyarenko, M V Kossov and H -P. Wellisch. "Chiral invariant phase space event generator". In: *The European Physical Journal A* 8.2 (2000), pp. 217–222. ISSN: 1434-601X. DOI: 10.1007/s100500070108. URL: https://doi.org/10.1007/s100500070108.

[8] M Kossov. "Simulation of antiproton-nuclear annihilation at rest". In: *IEEE Transactions on Nuclear Science* 52.6 (2005), pp. 2832–2835. DOI: 10.1109/TNS.2005.862878.

[9] B Andersson, G Gustafson and B Nilsson-Almqvist. "A model for low-pT hadronic reactions with generalizations to hadron-nucleus and nucleus-nucleus collisions". In: *Nuclear Physics* 281 (1987), pp. 289–309. DOI: 10.1016/0550-3213(87)90257-4.

[10] Bo Nilsson-Almqvist and Evert Stenlund. "Interactions Between Hadrons and Nuclei: The Lund Monte Carlo-Fritiof Version 1.6". In: *Computer Physics Communications* 43 (1987), pp. 387–397. DOI: 10.1016/0010-4655(87)90056-7.

[11] A. Galoyan and V. Uzhinsky. "Simulations of light antinucleus-nucleus interactions". In: *Hyperfine Interactions* 215.1-3 (Mar. 2013), pp. 69–76. ISSN: 03043843. DOI: 10.1007/s10751-013-0780-2.

[12] A Fasso et al. "The Physics models of FLUKA: Status and recent developments". In: *eConf* C0303241 (2003), MOMT005.

[13] T. T. Böhlen et al. "The FLUKA Code: Developments and Challenges for High Energy and Medical Applications". In: *Nuclear Data Sheets* 120 (June 2014), pp. 211–214. ISSN: 0090-3752. DOI: 10.1016/J.NDS.2014.07.049.

[14] S. Aghion et al. "Measurement of antiproton annihilation on Cu, Ag and Au with emulsion films". In: *Journal of Instrumentation* 12.4 (Apr. 2017). ISSN: 17480221. DOI: 10.1088/1748-0221/12/04/P04021.

[15] X. Llopart et al. "Timepix4, a large area pixel detector readout chip which can be tiled on 4 sides providing sub-200 ps timestamp binning". In: *Journal of Instrumentation*. Vol. 17. 1. IOP Publishing Ltd, Jan. 2022. DOI: 10.1088/1748-0221/17/01/C01044.

[16] Eberhard Klempt, Chris Batty and Jean Marc Richard. "The antinucleon-nucleon interaction at low energy: Annihilation dynamics". In: *Physics Reports* 413.4-5 (July 2005), pp. 197–317. ISSN: 03701573. DOI: 10.1016/j.physrep.2005.03.002.

[17] D. Gotta et al. "X-ray transitions from antiprotonic noble gases". In: *European Physical Journal D* 47.1 (2008), pp. 11–26. ISSN: 14346079. DOI: 10.1140/epjd/e2008-00025-3.

[18] H S Plendl et al. "Antiproton-nucleus annihilation at rest". In: *Physica Scripta* 48.2 (1993), pp. 160–163. ISSN: 0031-8949. URL: http://inis.iaea.org/search/search.aspx?orig_q=RN:25012806.

[19] M. Hori and J. Walz. "Physics at CERN's antiproton decelerator". In: *Progress in Particle and Nuclear Physics* 72 (Sept. 2013), pp. 206–253. ISSN: 01466410. DOI: 10.1016/j.ppnp.2013.02.004.

[20] Walter Oelert. "The elena project at CERN". In: *Acta Physica Polonica B*. Vol. 48. 10. Jagellonian University, Oct. 2017, pp. 1895–1902. DOI: 10.5506/APhysPolB.48.1895.

[21] Y.Bylinsky, A.M.Lombardi and W.Pirkl. "RFQD - a Decelerating Radio Frequency Quadrupole for the CERN Antiproton Facility". In: 2000.

[22] Vinod Chohan et al. *Extra Low ENergy Antiproton (ELENA) ring and its Transfer Lines: Design Report*. CERN Yellow Reports: Monographs. Geneva: CERN, 2014. DOI: 10.5170/CERN-2014-002. URL: https://cds.cern.ch/record/1694484.

[23] M Hori and E Widmann. *Status report of the ASACUSA experiment - progress in 2021 and plans for 2022*. Tech. rep. Geneva: CERN, 2022. URL: https://cds.cern.ch/record/2799130.

[24] N. Kuroda et al. "Development of a monoenergetic ultraslow antiproton beam source for high-precision investigation". In: *Physical Review Special Topics - Accelerators and Beams* 15.2 (Feb. 2012). ISSN: 10984402. DOI: 10.1103/PhysRevSTAB.15.024702.

[25] J. Fajans and C. M. Surko. "Plasma and trap-based techniques for science with antimatter". In: *Physics of Plasmas* 27.3 (Mar. 2020). ISSN: 10897674. DOI: 10.1063/1.5131273.

[26] Naofumi Kuroda. "Accumulation of a large number of antiprotons and production of an ultra-slow antiproton beam". PhD thesis. University of Tokyo, 2003. URL: https://radphys4.c.u-tokyo.ac.jp/theses/PhD/Kuroda-dthes.pdf.

[27] Minori Tajima. "Development of injection scheme of antiprotons and production of antihydrogen atoms in low-lying excited states". PhD thesis. University of Tokyo, 2017. URL: https://radphys4.c.u-tokyo.ac.jp/theses/PhD/Tajima-dthes.pdf.

[28] Poul Dähl. *Introduction to ELECTRON AND ION OPTICS*. 1973. ISBN: ISBN0-12-200650-X.

[29] David J Manura and David A. Dahl. *SIMION Version 8.0/8.1 User Manual*. Document Revision 5. Ringoes, NJ: Scientific Instrument Services, Inc, 2011.

[30] Scientific Instrument Services Inc. *SIMION 8.1 Supplemental Documentation*. 2013. URL: https://simion.com/info/8.1/docs/supplemental/.

[31] Miklos Szilagyi. *Electron and Ion Optics*. Springer US, 1988. ISBN: 978-1461282471. DOI: 10.1007/978-1-4613-0923-9.

[32] Ingo Hofmann. "Performance of solenoids versus quadrupoles in focusing and energy selection of laser accelerated protons". In: *Physical Review Special Topics - Accelerators and Beams* 16.4 (Apr. 2013). ISSN: 10984402. DOI: 10.1103/PhysRevSTAB.16.041302.

[33] Eric Giglio. *Boundary Conditions in SIMION*. 2015. URL: https://simion.com/docs/ganil-2015/paper_eric_giglio.pdf.

[34] E Widmann and M Hori. *ASACUSA STATUS REPORT Recent progress and plans for LS2*. Tech. rep. Geneva: CERN, 2019. URL: https://cds.cern.ch/record/2654222.

[35] Eberhard Widmann. *ASACUSA STATUS REPORT Recent progress and plans for 2018*. Tech. rep. Geneva: CERN, 2018. URL: http://cds.cern.ch/record/2300138.

[36] N Kuroda et al. "Radial Compression of an Antiproton Cloud for Production of Intense Antiproton Beams". In: *Physical Review Letters* 100.20 (May 2008), p. 203402. DOI: 10.1103/PhysRevLett.100.203402. URL: https://link.aps.org/doi/10.1103/PhysRevLett.100.203402.

[37] P. R. Mahaffy and K. Lai. "An electrostatic quadrupole deflector for mass spectrometer applications". In: *Journal of Vacuum Science & Technology A: Vacuum, Surfaces, and Films* 8.4 (July 1990), pp. 3244–3246. ISSN: 0734-2101. DOI: 10.1116/1.576571.

[38] H. D. Zeman. "Deflection of an ion beam in the two-dimensional electrostatic quadrupole field". In: *Review of Scientific Instruments* 48.8 (1977), pp. 1079–1085. ISSN: 00346748. DOI: 10.1063/1.1135188.

[39] Omer Sise, Melike Ulu and Mevlut Dogan. "Multi-element cylindrical electrostatic lens systems for focusing and controlling charged particles". In: *Nuclear Instruments and Methods in Physics Research Section A: Accelerators, Spectrometers, Detectors and Associated Equipment* 554.1-3 (Dec. 2005), pp. 114–131. ISSN: 0168-9002. DOI: 10.1016/J.NIMA.2005.08.068.

[40] Pierre Chauveau. *SIMION's Simplex optimizer applied to electrode's potential and geometry.* 2015. URL: https://simion.com/docs/ganil-2015/paper_pierre_chauveau.pdf.

[41] Kerry Cheung, Luis Fernando Velásquez-García and Akintunde Ibitayo Akinwande. "Chip-scale quadrupole mass filters for portable mass spectrometry". In: *Journal of Microelectromechanical Systems* 19.3 (June 2010), pp. 469–483. ISSN: 10577157. DOI: 10.1109/JMEMS.2010.2046396.

[42] Gertrude F. Rempfer. "Unipotential electrostatic lenses: Paraxial properties and aberrations of focal length and focal point". In: *Journal of Applied Physics* 57.7 (1985), pp. 2385–2401. ISSN: 00218979. DOI: 10.1063/1.334347.

[43] P. Mandal, G. Sikler and M. Mukherjee. "Simulation study and analysis of a compact einzel lens-deflector for low energy ion beam". In: *Journal of Instrumentation* 6.2 (Feb. 2011). ISSN: 17480221. DOI: 10.1088/1748-0221/6/02/P02004.

[44] Pintu Mandal, G Sikler and Manas Mukherjee. "An einzel lens with a diagonal-slit central electrode to combine steering and focusing of a low energy ion beam". In: *arXiv: Nuclear Experiment* (2010).

[45] M H Rashid. "Simple analytical method to design electrostatic einzel lens". In: *DAE Symp. Nucl. Phys.* 56 (2011), pp. 1132–1133.

[46] Andrew Christensen et al. "Patch Potential Induced Particle Loss in an Antimatter Penning-Malmberg Trap". In: *APS Division of Plasma Physics Meeting Abstracts.* Vol. 2019. APS Meeting Abstracts. Jan. 2019, GP10.015.

[47] Jie Li et al. "Electron-induced secondary electron emission of aluminum alloy processed via the combination of alodine treatment and carbon film deposition". In: *Materials Letters* 327 (Nov. 2022). ISSN: 18734979. DOI: 10.1016/j.matlet.2022.133085.

Acronyms

$\boldsymbol{E}_{\mathsf{kin}}$ kinetic energy. 5, 6, 8, 12, 17, 20

$\boldsymbol{E}_{\mathsf{pot}}$ potential energy. 12

$\overline{\mathsf{H}}$ antihydrogen. 7, 9, 30

$\overline{\mathsf{p}}$ antiprotons. vii, 3, 4, 6–8, 11, 12, 21–23, 25, 26, 36–38, 43, 44, 46, 50, 52, 53, 56, 59, 60, 71, 73, 75

$\overline{\mathsf{p}}\mathsf{A}$ antiproton-nucleus. 1, 2

$\overline{\mathsf{p}}\mathsf{N}$ antiproton-nucleon annihilation. 3

e^+ positron. 2, 8, 44, 55, 71

e^- electron. 2, 6, 11

$\mathsf{p}\overline{\mathsf{p}}$ proton-antiproton annihilation. 3

$\vec{\boldsymbol{B}}$ magnetic field. 17

AD Antiproton Decelerator. 1, 4–7, 21, 59, 71

AEGIS Antihydrogen Experiment: Gravity, Interferometry, Spectroscopy. 2, 71

ASACUSA Atomic Spectroscopy And Collisions Using Slow Antiprotons. 2, 4, 7, 8, 21, 60, 71

BO-PET biaxially oriented polyethylene terephtalate. 8

CERN European Organization for Nuclear Research. 1, 2, 5, 71

CHIPS Chiral Invariant Phase Space model. iii, 1

CPT charge parity time. 1, 7

DC direct current. 12

DCE downstream catching electrode. 11

E1 Einzel lens 1. 30, 32, 37–40, 42–44, 50, 51, 53, 59, 69, 74

E2 Einzel lens 2. 30, 32, 39, 40, 42–44, 50, 51, 53, 56, 59, 69, 74, 75

E3 Einzel lens 3. 30, 39, 43, 44, 46, 49–51, 53, 59, 74

EE extraction electrodes. 12, 22, 24

ELENA Extra Low Energy Antiproton ring. vii, 5–8, 21, 59, 71

FEM finite element method. 22

FLUKA Fluktuierende Kaskade model. 1

FTFP Fritiof precompound model. iii, 1

GEANT4 Geometry and Tracking. 1

GU graphical unit. 18, 22, 27, 40, 42, 54, 74

GUI graphical user interface. 19

GV gate valves. 13, 43, 44, 46, 47, 71, 74

HIP heavily ionizing particles. 1, 2, 71

KDE Kernel density estimate. 53, 75

MCP multi channel plate. 60

MIP minimum ionizing particles. 1, 2, 71

MRE multi ring electrode trap. 7, 9–12, 22–24, 69, 71, 72

MUSASHI Monoenergetic Ultra Slow Antiproton Source for High-precision Investigations. vii, 7–13, 21–26, 30, 31, 37, 38, 43, 44, 46, 51, 53, 54, 59, 69, 71–73

PA potential array. vii, 18–20, 22, 23, 28, 31, 32, 40, 42, 53, 72, 74

PE potential energy. 25, 27–29, 36, 37, 72, 73

PEANUT Cascade-Preequilibrium model. 1

PEEK polyetheretherketone. 34, 43, 55, 73, 75

PS Proton Synchrotron. 6

RF radio frequency. 6

RFQD radio frequency quadrupole decelarator. 7, 8

SEE secondary electron emission. 55

SEY secondary electron yield. 55

SM standard model of particle physics. 1

SMI Stefan Meyer Institute. 60

UCE upstream catching electrode. 11, 24

UHV ultra high vacuum. 55

List of Tables

List of Figures

A. Technical Drawings

11059-Slow-Extraction
11059-13-Setup

Anzahl: 1 Stück
M 1:2

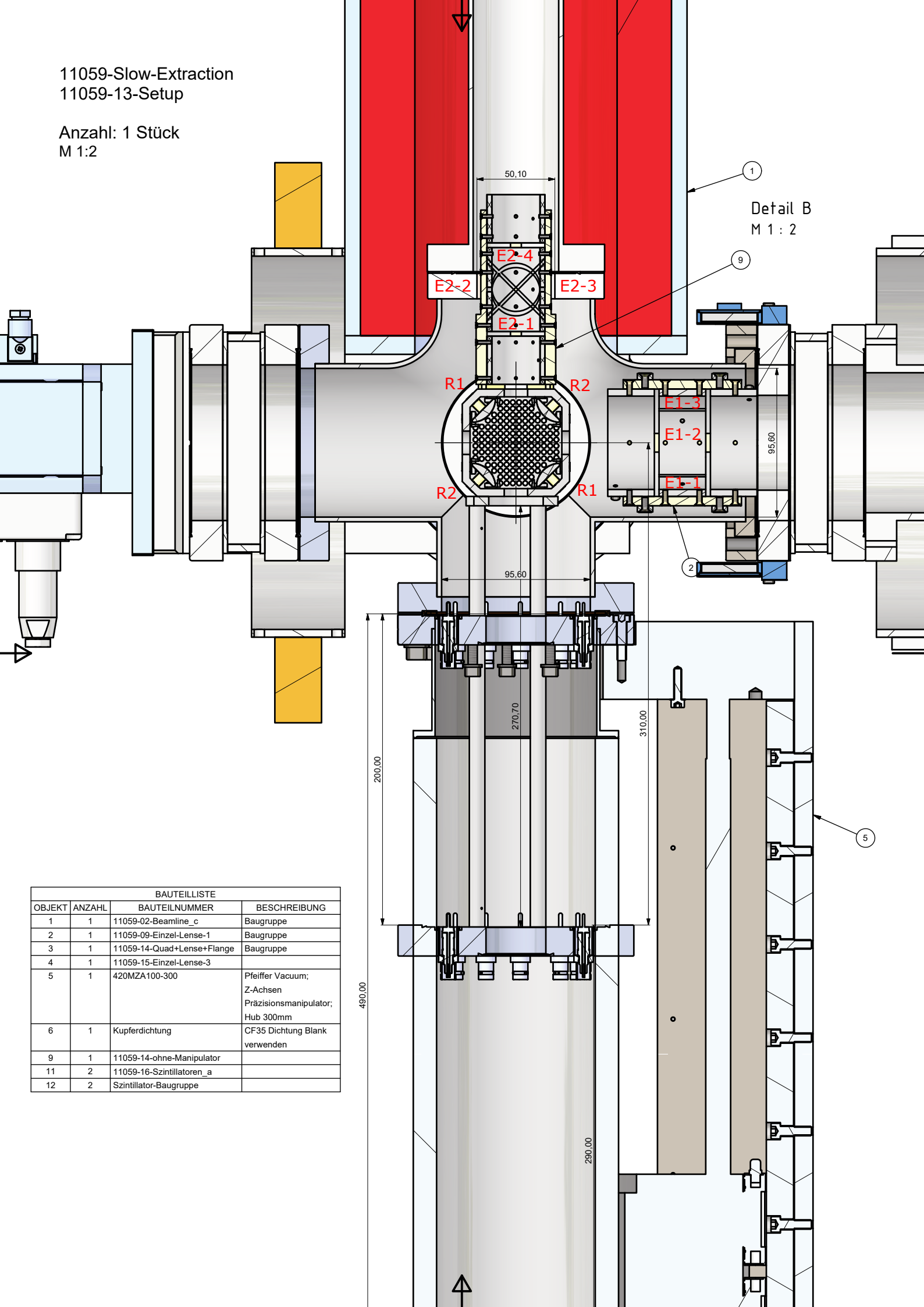

BAUTEILLISTE			
OBJEKT	ANZAHL	BAUTEILNUMMER	BESCHREIBUNG
1	1	11059-02-Beamline_c	Baugruppe
2	1	11059-09-Einzel-Lense-1	Baugruppe
3	1	11059-14-Quad+Lense+Flange	Baugruppe
4	1	11059-15-Einzel-Lense-3	
5	1	420MZA100-300	Pfeiffer Vacuum; Z-Achsen Präzisionsmanipulator; Hub 300mm
6	1	Kupferdichtung	CF35 Dichtung Blank verwenden
9	1	11059-14-ohne-Manipulator	
11	2	11059-16-Szintillatoren_a	
12	2	Szintillator-Baugruppe	

11059-Slow-Extraction
11059-13-Setup

11059-09-Einzel-Lense-1
Anzahl: 1 Stück
M 1:1

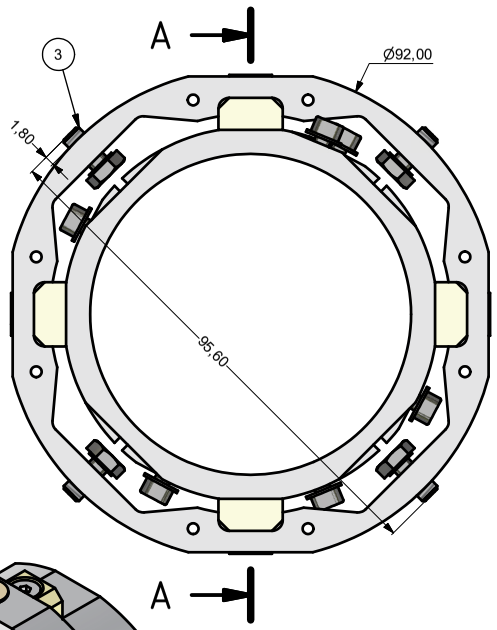

Schnitt A-A
M 1 : 1

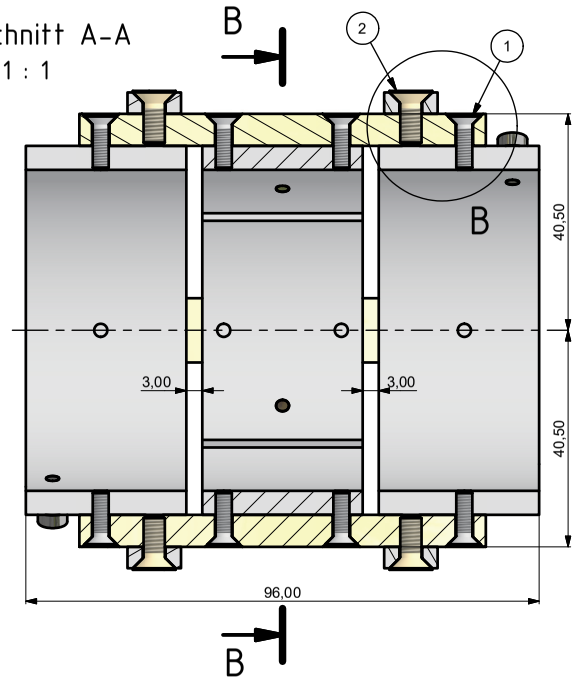

Schnitt B-B
M 1 : 1

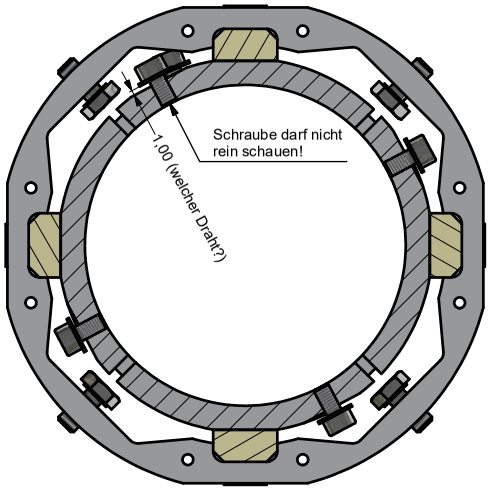

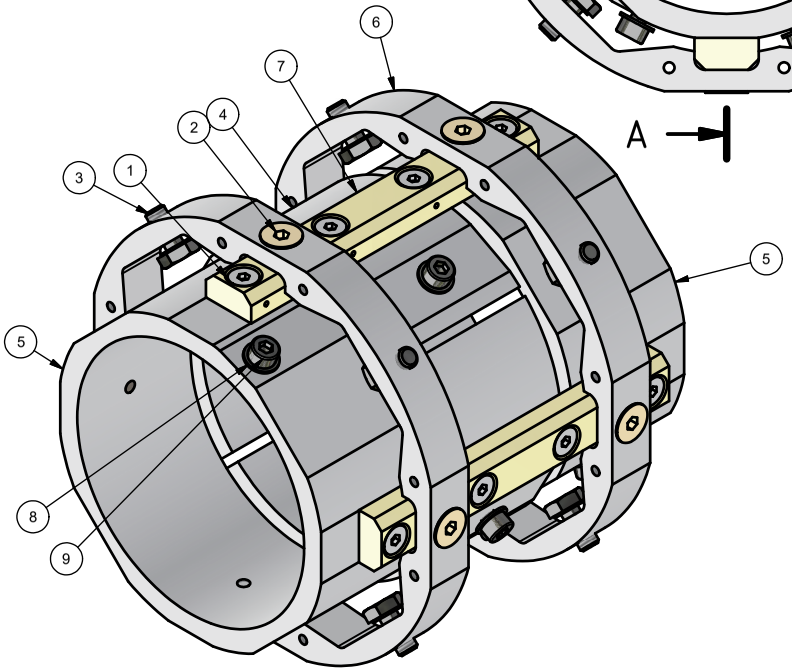

Detail B
M 3: 1

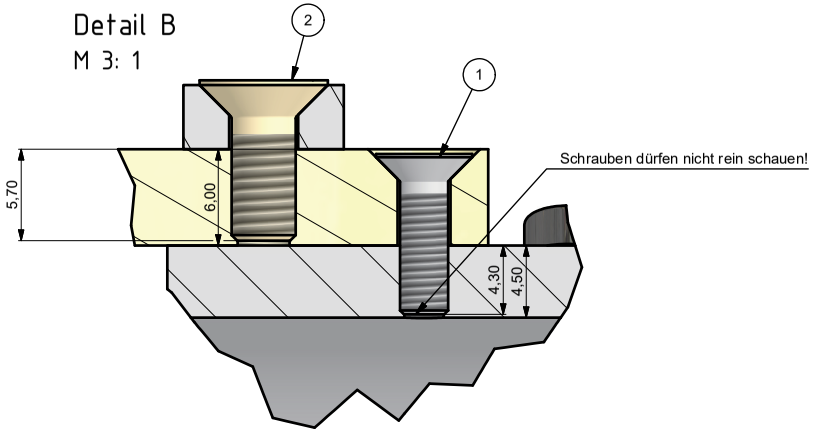

BAUTEILLISTE

OBJEKT	ANZAHL	Notizen	BAUTEILNUMMER	BESCHREIBUNG	MATERIAL
1	16		DIN 7991 - M3x10	Senkschrauben mit Innensechskant	Edelstahl A4
2	8	entlüftet	DIN 7991 - M4x10	Senkschrauben mit Innensechskant	PEEK
3	8	Gewinde bis zum Kopf	DIN 933 - M4 x 8	Sechskantschraube	Edelstahl A4
4	1		Einzel-Lense-5		Aluminium
5	2		Einzel-Lense-4		Aluminium
6	2		Montagering		Aluminium
7	4		Montagestab-1		TECAPEEK GF30
8	6		ISO 7089 - 3	Unterlegscheiben	Edelstahl A4
9	6	eventuell M3x5	DIN 912 - M3 x 6	Zylinderkopfschraube	Edelstahl A4

Stefan-Meyer-Institut
für subatomare Physik
Österreichischen Akademie der Wissenschaften

Kegelgasse 27
A-1030 Wien
Tel: (+43 1) 515 81 4520
www.oeaw.ac.at/smi

Status	Änderungen	Datum	Name

	Datum	Name
Gezeichnet	02.08.2022	Doris

11059-09-Einzel-Lense-1

1
A3

11059-Slow-Extraction
11059-14-Quad+Lense+Flange

Anzahl: 1 Stück
M 1:1

Schnitt A-A
M 1 : 1

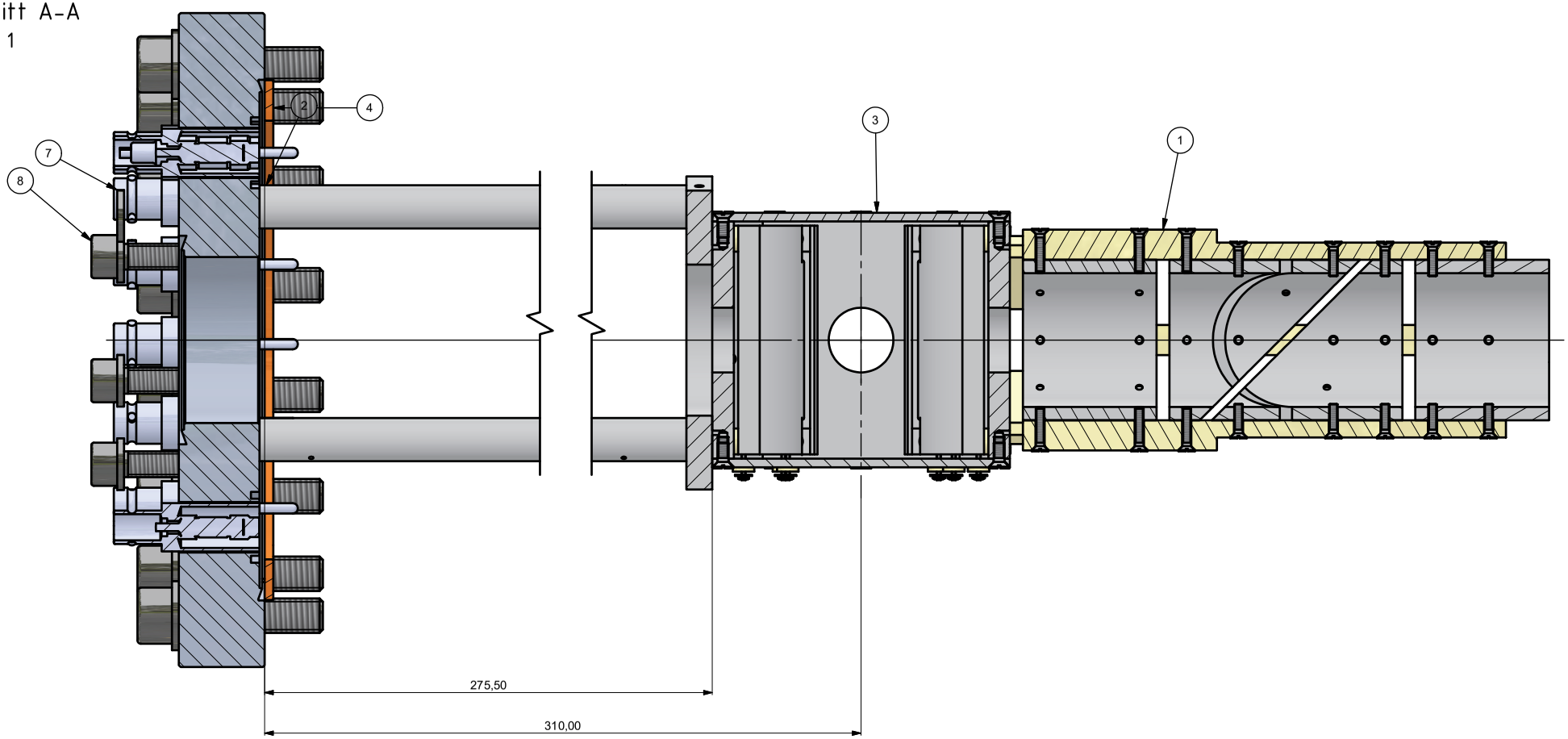

BAUTEILLISTE

OBJEKT	ANZAHL	Notizen	BAUTEILNUMMER	BESCHREIBUNG	MATERIAL	MASSE
1	1		11059-10-Einzel-Lense-2	Baugruppe		0,153 kg
2	1		11059-12-CF100	Baugruppe		0,559 kg
3	1		11059-08-Quad_d	Baugruppe		0,277 kg
4	1		Hositrad_CG100	STEP AP214	OFHC Kupfer	0,007 kg
5	16		ISO 7089 - 8	Unterlegscheiben	A4 Edelstahl	0,002 kg
6	16		DIN 912 - M8 x 35	Zylinderkopfschraube	A4 Edelstahl	0,021 kg
7	6		ISO 7089 - 6	Unterlegscheiben	A4 Edelstahl	0,001 kg
8	6		DIN 912 - M6 x 25	Zylinderkopfschraube	A4 Edelstahl	0,009 kg

Stefan-Meyer-Institut
für subatomare Physik
Österreichischen Akademie der Wissenschaften

Kegelgasse 27
A-1030 Wien
Tel: (+43 1) 515 81 4520
www.oeaw.ac.at/smi

Status	Änderungen	Datum	Name

	Datum	Name
Gezeichnet	02.08.2022	Doris

11059-14-Quad+Lense+Flange

1

A3

11059-Slow-Extraction
11059-13-Setup

11059-09-Einzel-Lense-3
Anzahl: 1 Stück
M 1:1

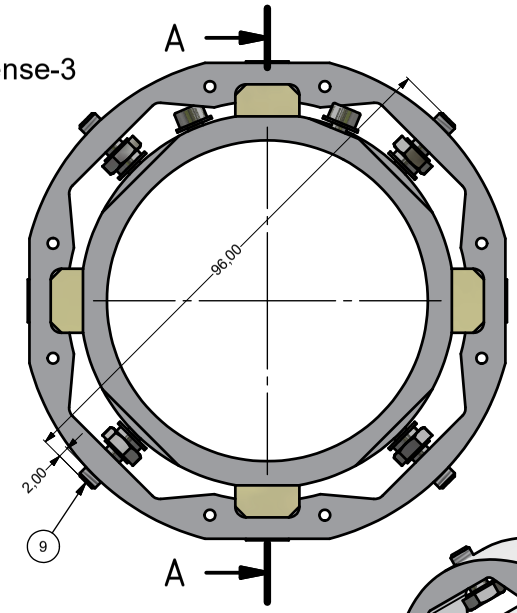

Schnitt A-A
M 1 : 1

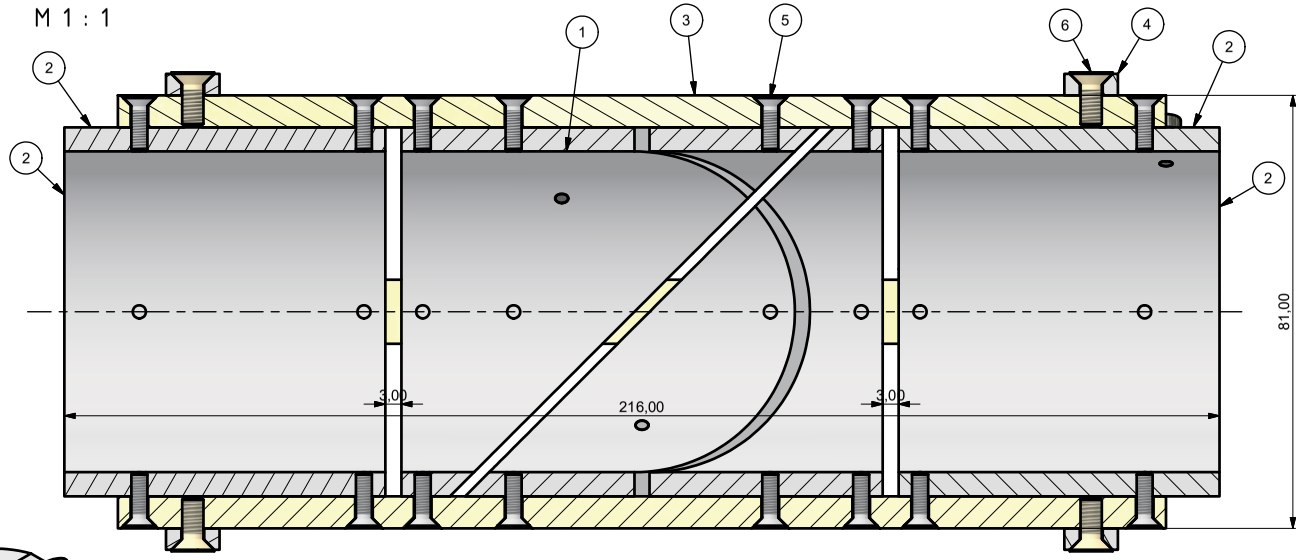

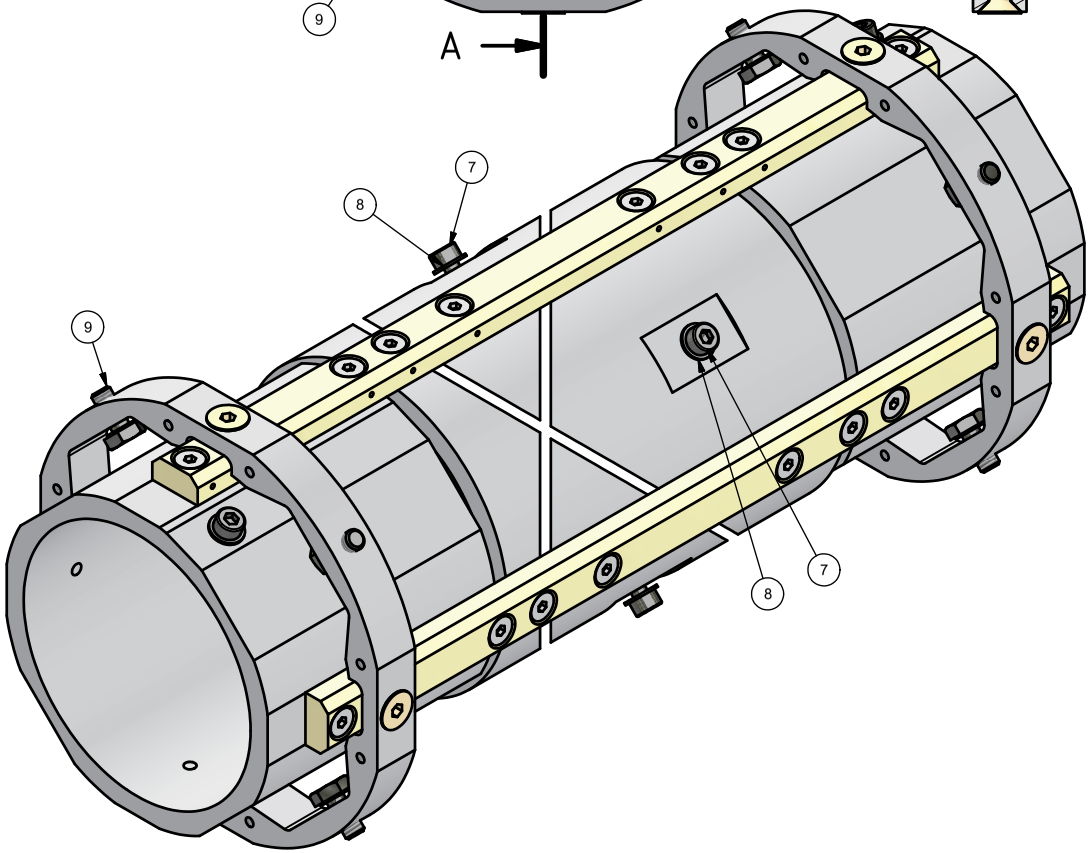

BAUTEILLISTE					
OBJEKT	ANZAHL	Notizen	BAUTEILNUMMER	BESCHREIBUNG	MATERIAL
1	1		Einzel-Lense-7		Aluminium
2	2		Einzel-Lense-6		Aluminium
3	4		Montagestab-4		TECAPEEK GF30
4	2		Montagering		Aluminium
5	32		DIN 7991 - M3x10	Senkschrauben mit Innensechskant	Edelstah A4
6	8	entlüften	DIN 7991 - M4x10	Senkschrauben mit Innensechskant	PEEK
7	6	eventuell M3x5	DIN 912 - M3 x 6	Zylinderkopfschraube	Edelstahl A4
8	6		ISO 7089 - 3	Unterlegscheiben	Edelstahl A4
9	8	Gewinde bis Kopf	DIN 933 - M4 x 8	Sechskantschraube	Edelstahl A4

Stefan-Meyer-Institut
für subatomare Physik
Österreichischen Akademie der Wissenschaften

Kegelgasse 27
A-1030 Wien
Tel: (+43 1) 515 81 4520
www.oeaw.ac.at/smi

	Datum	Name
Gezeichnet	02.08.2022	Doris

Status	Änderungen	Datum	Name

11059-15-Einzel-Lense-3

1
A3